



141  
888  
THS

LIBRARY  
Michigan State  
University

This is to certify that the  
dissertation entitled

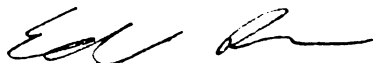
NUCLEAR REACTIONS IN TYPE IA SUPERNOVAE:  
EFFECTS OF PROGENITOR COMPOSITION AND  
DETONATION ASYMMETRY

presented by

David A. Chamulak

has been accepted towards fulfillment  
of the requirements for the

Ph.D. degree in Physics



Major Professor's Signature

8.21.09

Date

*MSU is an Affirmative Action/Equal Opportunity Employer*



NUCLEAR REACTIONS IN TYPE IA SUPERNOVAE: EFFECTS OF  
PROGENITOR COMPOSITION AND DETONATION ASYMMETRY

By

David A. Chamulak

A DISSERTATION

Submitted to  
Michigan State University  
in partial fulfillment of the requirements  
for the degree of

DOCTOR OF PHILOSOPHY

Physics

2009

## ABSTRACT

### NUCLEAR REACTIONS IN TYPE IA SUPERNOVAE: EFFECTS OF PROGENITOR COMPOSITION AND DETONATION ASYMMETRY

By

David A. Chamulak

Type Ia supernovae go through three distinct phases before their progenitor star is obliterated in a thermonuclear explosion. First is “simmering,” during which the  $^{12}\text{C} + ^{12}\text{C}$  reaction gradually heats the white dwarf on a long ( $\sim 10^3$  yr) timescale. Next is a period of subsonic burning. Finally, a detonation is thought to occur that finishes unbinding the star. This thesis investigates the nuclear reactions that take place in these three phases and considers what that may be able to tell us about the progenitor systems and the mechanics behind the detonation. First, we investigate the nuclear reactions during this simmering with a series of self-heating, at constant pressure, reaction network calculations. As an aid to hydrodynamical simulations of the simmering phase, we present fits to the rates of heating, electron capture, change in mean atomic mass, and consumption of  $^{12}\text{C}$  in terms of the screened thermally averaged cross section for  $^{12}\text{C} + ^{12}\text{C}$ . Our evaluation of the net heating rate includes contributions from electron captures into the 3.68 MeV excited state of  $^{13}\text{C}$ . We compare our one-zone results to more accurate integrations over the white dwarf structure to estimate the amount of  $^{12}\text{C}$  that must be consumed to raise the white dwarf temperature, and hence to determine the net reduction of  $Y_e$  during simmering. Second, we consider the effects of  $^{22}\text{Ne}$  on flame speed. Carbon-oxygen white dwarfs contain  $^{22}\text{Ne}$  formed from  $\alpha$ -captures onto  $^{14}\text{N}$  during core He burning in the progenitor star. In a white dwarf (type Ia) supernova, the  $^{22}\text{Ne}$  abundance determines, in part, the neutron-to-proton ratio and hence the abundance of radioactive  $^{56}\text{Ni}$  that powers the lightcurve. The  $^{22}\text{Ne}$  abundance also changes the burning rate and hence the laminar flame speed. We tabulate the flame speedup for different initial  $^{12}\text{C}$  and  $^{22}\text{Ne}$  abun-

dances and for a range of densities. This increase in the laminar flame speed --about 30% for a  $^{22}\text{Ne}$  mass fraction of 6%—affects the deflagration just after ignition near the center of the white dwarf, where the laminar speed of the flame dominates over the buoyant rise, and in regions of lower density  $\sim 10^7 \text{ g cm}^{-3}$  where a transition to distributed burning is conjectured to occur. The increase in flame speed will decrease the density of any transition to distributed burning. Finally, we look at how a surface detonation affects the composition of nuclides across the supernovae remnant. Several scenarios have been proposed as to how this delayed detonation may actually occur but careful nucleosynthesis calculations to determine the isotopic abundances produced by these scenarios have not been done. The surface detonation produces a clear compositional gradient in elemental Ni in layers of the white dwarf that do not burn to nuclear statistical equilibrium (NSE). A number of nuclides show a gradient but when combined into elemental abundances Ni shows the largest change over the face of the star. The Ni abundance varies by as much as an order of magnitude across the star. This may be a way to observationally test detonation models.

## DEDICATION

To the men who understand—or think they do

Allen W. Jackson, *The Half Timber House*

## ACKNOWLEDGMENT

Special thanks goes to my advisor Ed Brown; my committee members, Tim Beers, Kirsten Tollefson, Mark Voit, and Remco Zegers; collaborators, Frank Timmes, Casey A. Meakin, Ivo Seitzzahl, James Truran; For all the Physics and Astronomy graduate students at Michigan State, and for every one else who was there for me over these last 10 years in College.

# TABLE OF CONTENTS

<b>List of Tables</b> . . . . .	vii
<b>List of Figures</b> . . . . .	viii
<b>1 Introduction</b> . . . . .	<b>1</b>
1.1 Compositional Effects . . . . .	3
1.2 Detonation . . . . .	5
<b>2 Methodology</b> . . . . .	<b>6</b>
2.1 Thermonuclear cross sections and reaction rates . . . . .	6
2.2 Reaction networks . . . . .	9
<b>3 Electron captures in simmering</b> . . . . .	<b>11</b>
3.1 Introduction . . . . .	11
3.2 The reduction in electron abundance during the explosion . . . . .	13
3.2.1 The role of neon-22 and other trace nuclides . . . . .	14
3.2.2 The reaction $^{13}\text{N}(e^-, \nu_e)^{13}\text{C}$ . . . . .	16
3.2.3 Production and subsequent captures of neutrons . . . . .	18
3.3 Reaction network calculations . . . . .	19
3.3.1 The reactive flows . . . . .	20
3.3.2 The effective $Q$ -value of the $^{12}\text{C} + ^{12}\text{C}$ reaction . . . . .	26
3.3.3 Heating of the white dwarf core and the end of simmering . . . . .	29
3.4 Discussion and conclusions . . . . .	34
<b>4 The effect of <math>^{22}\text{Ne}</math> on flame speed</b> . . . . .	<b>39</b>
4.1 Introduction . . . . .	39
4.2 The laminar flame . . . . .	40
4.3 Results . . . . .	43
4.4 Discussion . . . . .	47
<b>5 Compositional effects of surface detonation</b> . . . . .	<b>49</b>
5.1 Introduction . . . . .	49
5.2 The Explosion Model . . . . .	49
5.3 Results . . . . .	52
5.4 Discussion . . . . .	57
<b>6 Conclusion</b> . . . . .	<b>58</b>
<b>Bibliography</b> . . . . .	<b>61</b>

## LIST OF TABLES

3.1	430-Nuclide Reaction Network . . . . .	19
3.2	Change in electron abundance per carbon consumed during the pre-explosion convective burning . . . . .	26
4.1	Laminar flame speed and width . . . . .	44
5.1	493-Nuclide Reaction Network . . . . .	52
5.2	Partial table of nuclides that do and do not display a separation because of asymmetric detonation. . . . .	53

## LIST OF FIGURES

Images in this dissertation are presented in color

3.1	Thermally averaged cross-sections as a function of temperature . . . .	17
3.2	Reaction flows at $\rho = 10^9 \text{ g cm}^{-3}$ . . . . .	22
3.3	Reaction flows at $\rho = 3 \times 10^9 \text{ g cm}^{-3}$ . . . . .	23
3.4	Change in electron abundance as a function of carbon consumed . . .	30
3.5	Convective and electron capture timescales as a function of temperature	33
3.6	Correlation between $12 + \log(\text{O}/\text{H})$ and $\Delta m_{15}(B)$ induced by the electron abundance . . . . .	36
4.1	Flame speed as a function of density . . . . .	42
4.2	Abundances of selected nuclides during a burn at $\rho = 2.0 \times 10^9 \text{ g cm}^{-3}$	45
5.1	Final abundance of elemental Ni as a function of central angle . . . .	54
5.2	Thermal expansion time scale as a function of initial position . . . .	55
5.3	Final abundance of elemental Ni as a function of radial velocity . . .	56

# Chapter 1

## Introduction

In the pantheon of astronomical explosions few are as bright as the Type Ia supernova (hereafter SNe Ia). SNe Ia are, by definition, a category of variable stars that lack hydrogen and present a singly ionized silicon line (in the rest frame) at 615.0 nm in their spectrum near peak light. There are several ways by which a supernova of this type could form, but all share a common underlying mechanism. Stars with a main sequence mass between approximately 0.8-8 solar masses first consume hydrogen and form helium. Helium is built up in the core of the star until it too starts to burn, at which time the star enters its giant phase of evolution. During the giant phase the star fuses the helium in the core to carbon and oxygen. Since the mass of the star is less than 8 solar masses it is not able to continue to burn carbon to neon and magnesium and becomes a carbon-oxygen white dwarf, once the helium is consumed. Stars between 8 and 10 solar masses can burn carbon and become oxygen-neon-magnesium white dwarfs. When a slowly-rotating, carbon-oxygen (C-O) white dwarf accretes matter from a companion, it cannot exceed the Chandrasekhar limit of approximately 1.38 solar masses, beyond which it would no longer be able to support itself through electron degeneracy pressure and begin to collapse. In the absence of a countervailing process, the white dwarf would collapse to form a neutron star, as is

thought to occur in the case of an oxygen-neon-magnesium white dwarf.

As described in Hillebrandt & Niemeyer (2000), the increase in pressure and density due to the increasing mass raises the temperature of the core. Once the temperature and density of the core is such that the heating from carbon burning is greater than the energy loss from thermal neutrinos, a period of convective burning ensues, lasting approximately 1,000 years. This phase of burning is known as the “simmering” phase. Once burning has begun, the temperature of the white dwarf starts to rise. A star, like the sun, supported by thermal pressure would expand and cool in order to counter-balance an increase in thermal energy. However, since degeneracy pressure is independent of temperature; the white dwarf is unable to regulate the burning process in the same way. When the heating rate from carbon burning becomes faster than the sound crossing time of the star a subsonic deflagration flame front is born. The details of the ignition are still unknown, including the location and number of points where the flame begins. The flame accelerates dramatically, due to hot ash being Rayleigh-Taylor unstable to the surrounding cold, and therefore denser, fuel. The deflagration is hot enough to burn the C-O to iron group elements. At some point, it is thought, that the burning changes from a subsonic deflagration to a supersonic detonation, but the method by which happens is not well understood.

Regardless of the exact details of nuclear burning, it is generally accepted that a substantial fraction of the carbon and oxygen in the white dwarf is burned into heavier elements within a period of only a few seconds, raising the internal temperature to billions of degrees. This energy release from thermonuclear burning ( $\sim 10^{51}$  ergs) is more than enough to unbind the star.

Near the time of maximum luminosity, the spectrum contains lines of intermediate-mass elements from oxygen to calcium; these are the main constituents of the outer layers of the star. Months after the explosion, when the outer layers have expanded to the point of transparency, the spectrum is dominated by light emitted by material

near the core of the star, heavy elements synthesized during the explosion; most prominently iron peak elements. The radioactive decay of  $^{56}\text{Ni}$  through  $^{56}\text{Co}$  to  $^{56}\text{Fe}$  produces high-energy photons which dominate the energy output of the ejecta at intermediate to late times.

Type Ia supernovae have a characteristic light curve. The typical visual absolute magnitude of Type Ia supernovae is  $M_v = -19.3$  (Hillebrandt & Niemeyer, 2000). Because of this similarity, in the past decade SNe Ia have become the premier standard candle for measuring the geometry of the universe. Current observations are sampling the SNe Ia population out to a red shift,  $z \approx 1.6$  (Riess et al., 2004), and future missions will push this limit even farther to  $z \lesssim 2$ . The larger sample of SNe Ia carries with it the prospect for discovering the progenitors of these events and their evolution towards ignition. Numerical models (for a sampling of recent work, see Gamezo et al. 2004; Plewa et al. 2004; Röpke et al. 2006) are steadily becoming more refined and can begin to probe the connection between the properties of the progenitor white dwarf—its birth mass, composition, and binary companion—and the outcome of the explosion.

## 1.1 Compositional Effects

Despite the advances in modeling the post-ignition flame evolution (for a sampling of recent work, see Gamezo et al., 2004; Plewa et al., 2004; Röpke et al., 2006; Jordan et al., 2008), we still lack a complete understanding of which subset of the binary white dwarf population become SNe Ia, and how differences in the progenitor map onto differences in the outcome of the explosion.

The composition of the white dwarf at the time of the explosion should have an effect on the nucleosynthesis that takes place during the explosion and the isotopic abundances of the final composition. The observable properties of SNe Ia resulting

from Chandrasekhar-mass explosions are chiefly determined by their final composition, the velocity profiles of key spectral lines at early- and late-times (e.g., P-Cygni profiles of Si II at 615.0 nm at early times), the opacity of the material through which the photons from radioactive decay must propagate, the kinetic energy of ejecta, and its interaction with the density profile of the surrounding circumstellar or interstellar medium (Filippenko, 1997; Pinto & Eastman, 2000; Hillebrandt & Niemeyer, 2000; Leibundgut, 2001; Mazzali & Podsiadlowski, 2006; Marion et al., 2006; Blondin et al., 2006; Badenes et al., 2007; Woosley et al., 2007). The dominant parameter in setting the peak brightness, and hence width, of the light curve is widely believed to be the mass of  $^{56}\text{Ni}$  ejected by the explosion. Timmes et al. (2003) showed the mass of  $^{56}\text{Ni}$  produced depends linearly on the electron fraction,  $Y_e$ , at the time of the explosion, and that  $Y_e$  itself depends linearly on the abundance of  $^{22}\text{Ne}$  in the white dwarf.

The C:O ratio is set by the mass of the progenitor main-sequence star, although Röpke & Hillebrandt (2004) find that the C:O ratio is of secondary importance in setting the explosion energetics. After  $^{12}\text{C}$  and  $^{16}\text{O}$ , the next most abundant nuclide is  $^{22}\text{Ne}$ , which is synthesized via  $^{14}\text{N}(\alpha, \gamma)^{18}\text{O}(\alpha, \gamma)^{22}\text{Ne}$  during core He burning. The abundance of  $^{22}\text{Ne}$  is therefore proportional to the initial CNO abundance of the progenitor main sequence star. Timmes et al. (2003) showed that the mass of  $^{56}\text{Ni}$  synthesized depends *linearly* on the abundance of  $^{22}\text{Ne}$  at densities where electron capture rates are much slower than the explosion timescale,  $\sim 1$  s. Simulations with embedded tracer particles (Travaglio et al., 2004; Brown et al., 2005; Röpke et al., 2006) have confirmed this dependence.

These simulations studied the effect of adding  $^{22}\text{Ne}$  by post-processing the  $(\rho, T)$  traces, and as a result did not account for variations in either the progenitor structure or the sub-grid flame model caused by changes in the  $^{22}\text{Ne}$  abundance. One-dimensional studies that did attempt to incorporate different progenitors self-consistently (Höflich et al., 1998; Domínguez et al., 2001) found a much smaller dependence of the

$^{56}\text{Ni}$  yield on metallicity.<sup>1</sup>

## 1.2 Detonation

Besides effects from the progenitor white dwarf there is also a lack of understanding of the mechanics of how the star actually detonates. It is unclear how a SN Ia transitions from a subsonic deflagration to a supersonic detonation but simulations find a transition must occur since pure deflagration models do not burn enough of the white dwarf to account for any but the most subluminous events (Reinecke et al., 2002; Gamezo et al., 2004; Röpke et al., 2007a). Different models have been proposed to handle detonations in simulations (Khokhlov, 1988; Gamezo et al., 2004; Röpke et al., 2007b; Plewa et al., 2004; Plewa, 2007), however careful nucleosynthesis calculations to determine exact isotopic yields have not been done.

---

<sup>1</sup>It is unclear whether these studies allowed  $[\text{O}/\text{Fe}]$  to vary as a function of  $[\text{Fe}/\text{H}]$ .

# Chapter 2

## Methodology

Since all of the work covered in this thesis was completed using reaction networks this chapter will review reaction network methodology. This chapter is meant to only be primer in reaction network calculations, for a more detailed review of reaction network calculations see Timmes (1999).

### 2.1 Thermonuclear cross sections and reaction rates

Consider a reaction that takes the form  $j + k \rightarrow l$ . This reaction has a number of quantities associated with it; one being the cross section of the reaction,  $\sigma$ . The cross section gives the number of reactions per second per target per flux of incoming projectiles and may be directly measured through experiment, which can be difficult depending on the energy measured or the stability of the reactants. In such cases where  $\sigma$  can not be measured directly  $\sigma$  may be evaluated following a theoretical approach. A rate,  $r_{j,k}$ , for the reaction  $j + k \rightarrow l$  can be described by the equation

$$r_{j,k} = \int \sigma_{j,k} |v_j - v_k| d^3n_j d^3n_k, \quad (2.1)$$

where  $|v_j - v_k|$  is the relative velocity of  $j$  and  $k$  and  $n_j$  and  $n_k$  are the number densities of  $j$  and  $k$  respectively. This integral can be evaluated by specifying a distribution function. For example, take a Maxwell-Boltzmann distribution for  $j$  and  $k$

$$d^3n_j = n_j \left( \frac{m_j}{2\pi k_b T} \right)^{3/2} \exp \left( -\frac{m_j^2 v_j^2}{2k_b T} \right) d^3v_j, \quad (2.2)$$

where  $m_j$  is the mass of  $j$ ,  $k_b$  is the Boltzmann constant, and  $T$  is absolute temperature. If we transform from velocity to energy we can write the reaction rate as

$$r_{j,k} = \langle \sigma v \rangle_{j,k} n_j n_k, \quad (2.3)$$

where  $\langle \sigma v \rangle$  is the thermally averaged cross section defined as

$$\langle j, k \rangle \equiv \langle \sigma v \rangle_{j,k} = \left( \frac{8}{\mu\pi} \right) (k_b T)^{-3/2} \int_0^\infty E \sigma_{j,k}(E) \exp \left( -\frac{E}{k_b T} \right) dE, \quad (2.4)$$

where  $\mu$  is the reduced mass in the center of mass system. I have defined  $\langle j, k \rangle \equiv \langle \sigma v \rangle_{j,k}$  to eliminate confusion later when talking about one and three body reactions which I will designate by  $\langle j \rangle$  and  $\langle j, k, l \rangle$  respectively.

A similar technique can be used to find the reaction rate for a photodissociation of the form  $j + \gamma \rightarrow l + m$ . The velocities of the nuclei are always insignificant to that of light therefore the integrand in equation 2.1 is not dependent on  $d^3n_j$  and  $d^3n_k$  can be represented by a Planck distribution of photons. It is, however, very difficult to directly measure the cross section for a photodissociation and even if a cross section was somehow measured the inherent error would mean that equilibrium abundances would be off. It is therefore easier to calculate the photodissociation rate from the forward rate using detailed balance. This gives an equation  $r_j = \langle j \rangle n_j$  where

$$\langle j \rangle = \left( \frac{G_l G_m}{G_j} \right) \left( \frac{A_l A_m}{A_j} \right)^{3/2} \left( \frac{m_u k_b T}{2\pi \hbar^2} \right)^{3/2} \langle l, m \rangle \exp \left( \frac{-Q_{lm}}{k_b T} \right). \quad (2.5)$$

Here  $\langle l, m \rangle$  and  $Q_{lm}$  are the thermally averaged cross section and energy release of the reaction  $l + m \rightarrow j + \gamma$ ,  $A_l$  is the atomic mass of  $l$ ,  $m_u$  is the mass of a nucleon, and the partition functions  $G = \sum_i (2J_i + 1) \exp(-E_i/kT)$ .

For weak reactions, like for the case of photodissociation above, the velocity of the nuclei is insignificant since in the center of mass system,  $v_j \ll v_e$ ,  $|v_j - v_e| \approx |v_e|$ . Depending on the astrophysical conditions that one is interested in  $d^3n_e$  is either given by a Boltzmann distribution, partially degenerate distribution or Fermi distribution of electrons. It then follows that the electron capture rate is just a function of temperature,  $T$ , and number density,  $n_j$

$$r_j = \langle j \rangle (T, \rho Y_e) n_j. \quad (2.6)$$

Here  $Y_e$  is related to the number density of electrons,  $n_e$  by the equation  $Y_e = n_e / (\rho N_A)$ , where  $\rho$  is the density and  $N_A = 6.022 \times 10^{23} \text{ g}^{-1} = (1 \text{ amu})^{-1}$ .

A special consideration to take into account when calculating reaction rates is the effect of electron screening. In plasmas at high density or low temperature, the presence of background electrons and nuclei cause the reactant nuclei to feel a different Coulomb repulsion than they would if they were not surrounded by charged particles. If the change of the electrostatic potential,  $\phi$ , is such that  $\Delta\phi \ll kT$  the generalized reaction rate integral can be separated into the traditional expression (eq. 2.4) and a screening factor,  $f_{scr}$  (for a review of why this is see Salpeter & Van Horn, 1969), resulting in a new reaction rate  $\langle j, k \rangle^*$  such that,

$$\langle j, k \rangle^* = f_{scr} (Z_j, Z_k, \rho, T, Y_i) \langle j, k \rangle. \quad (2.7)$$

The screening factor is a function of the charges of the interacting nuclei,  $Z_j$  and  $Z_k$ , the density  $\rho$ , the temperature  $T$  and the composition of the plasma  $Y_i$ . For self

consistency a screening factor should be applied to a measured rate and the reverse rate should be calculated through detailed balance (Calder et al., 2007). This is the only way to be sure that material in equilibrium will have the right abundances when calculated with the network. This, however, is not always done and a screening factor often will be applied to a given forward and reverse rate resulting in a network run to equilibrium not preserving detailed balance.

## 2.2 Reaction networks

The number density of each nuclide in an astrophysical plasma at constant density varies with time according to the number of reactions per  $\text{cm}^3$  per second an expression given by

$$\left(\frac{\partial n_i}{\partial t}\right)_\rho = \sum_j N_j^i r_j + \sum_{j,k} N_{j,k}^i r_{j,k} + \sum_{j,k,l} N_{j,k,l}^i r_{j,k,l}. \quad (2.8)$$

here  $n_i$  is the number density of nuclide  $i$  and  $r$  is the reaction rate defined in § 2.1. The first sum is over all one body reactions such as decays, photodissociation, electron/positron captures and neutrino induced reactions. The second sum is over two body reactions like  $^{12}\text{C} + \alpha$ . The third sum is over three body reactions like the triple- $\alpha$  reactions. The  $N^i$ 's are defined as

$$N_j^i = N_i, \quad N_{j,k}^i = N_i / \prod_m |N_{jm}|!, \quad \text{and} \quad N_{j,k,l}^i = N_i / \prod_m |N_{jm}|! \quad (2.9)$$

Here  $N_i$  can be positive or negative and specifies how many particles of nuclide  $i$  are created or destroyed in a reaction. The products in the denominators, which include the factorials, run over the number of particles destroyed in a reaction and avoid double or triple counting reactions when like particles react with each other, like  $^{12}\text{C} + ^{12}\text{C}$  or the triple- $\alpha$  reactions.

For fluid equations the mass density is approximated as  $\rho = \sum_i n_i A_i \mu^{-1}$ , where

$\mu$  is the mass of one nucleon. The mass fraction of nuclide  $i$  is then  $X_i = n_i A_i \mu^{-1} \rho^{-1}$  and we can write  $n_i = (X_i/A_i) \mu \rho \equiv Y_i \mu \rho$ . This allows us to rewrite equation (2.8), in order to exclude changes in the number density which are only due to expansion or contraction of the gas, as

$$\dot{Y}_i = \sum_j N_j^i \langle j \rangle Y_j + \sum_{j,k} N_{j,k}^i \rho N_A \langle j, k \rangle Y_j Y_k + \sum_{j,k,l} N_{j,k,l}^i \rho^2 N_A^2 \langle j, k, l \rangle Y_j Y_k Y_l. \quad (2.10)$$

Here equation (2.10) follows directly from equation (2.8) when the definition for  $r$  and  $Y$  are introduced.

Therefore, it follows that the total energy generation per unit mass, due to reactions in a given time step which changes abundances by  $\Delta Y$  is

$$\varepsilon = -N_A \left[ c^2 \sum_i \left( M_i \frac{dY_i}{dt} \right) \right] - \varepsilon_\nu, \quad (2.11)$$

Here  $\varepsilon_\nu$  is the energy loss from neutrinos,  $M_i$  is the mass of nuclide  $i$  and  $c$  is the speed of light. Equations (2.10) form a series of stiff coupled ordinary differential equations, for which standard numerical solvers exist (see Press et al., 1992).

# Chapter 3

## Electron captures in simmering

### 3.1 Introduction

In this chapter we explore, using a reaction network coupled to an equation for self-heating at constant pressure, the reduction in  $Y_e$  that occurs after the onset of the thermonuclear runaway (when the heating from  $^{12}\text{C} + ^{12}\text{C}$  reactions is faster than cooling by thermal neutrino emission), but before the burning becomes so fast that local regions can thermally run away and launch a flame. This “simmering” epoch lasts for  $\sim 10^3$  yr, long enough that electron captures onto products of  $^{12}\text{C}$  burning can reduce the free electron abundance  $Y_e$ . A similar, but independent calculation, of the reduction of  $Y_e$  during simmering was performed by Piro & Bildsten (2008). Their calculation did not use a full reaction network, but it did take into account the change in energy of the white dwarf due to the growth of the convective zone. Our calculation agrees with their findings, in particular that there is a maximum  $Y_e$  at the time of the explosion, and that the reduction in  $Y_e$  is linear in the amount of  $^{12}\text{C}$  consumed prior to when the rate of  $^{12}\text{C}$  burning outpaces that of the weak reactions. This chapter expands on their work in three ways. First, by using a full reaction network, we are able to quantify the role of  $^{22}\text{Ne}$  and trace nuclides in setting the

change in electron abundance with  $^{12}\text{C}$  consumption,  $dY_e/dY_{12}$ . Second, we calculate the heating from the electron capture reactions and include the contribution from an excited state of  $^{13}\text{C}$ . Third, we provide tabulated expressions for the rate of heating  $\varepsilon$ , the rate of change in electron abundance  $dY_e/dt$ , and the rate of change in the mean atomic mass  $d\langle A \rangle/dt$  in terms of the reaction rate for the  $^{12}\text{C} + ^{12}\text{C}$  reaction. These expressions are useful input for large-scale hydrodynamical simulations of the simmering phase which do not resolve such microphysics.

We first give, in § 3.2, a simple estimate for the reduction in  $Y_e$  during the pre-explosion simmering and describe the role of  $^{22}\text{Ne}$  and other trace nuclides. In § 3.3 we describe our numerical calculations, explain the reactive flows that occur (§ 3.3.1), and give simple approximations to the heating rate and carbon consumption (§ 3.3.2). We detail, in § 3.3.3, some of the limitations of our approach. We evaluate the energy required to raise the white dwarf central temperature, and hence the amount of  $^{12}\text{C}$  that must be consumed, and compare it against the one-zone calculation. We also estimate the central temperature at which convective mixing becomes faster than electron captures. This convective mixing advects electron capture products to lower densities where they can  $\beta^-$ -decay: the convective Urca process. Because each electron capture-decay cycle emits a neutrino-anti-neutrino pair, there is energy lost from the white dwarf, and our calculation underestimates the amount of  $^{12}\text{C}$  consumed prior to the flame runaway. The convective Urca process (Paczynski, 1972) reduces the rate of heating by nuclear reactions (thereby increasing the amount of  $^{12}\text{C}$  that must be consumed to raise the temperature), but cannot result in a net decrease in entropy and temperature for constant or increasing density (Stein et al., 1999; Stein & Wheeler, 2006). The Urca reactions also tend to reduce the effects of buoyancy, and in degenerate matter have a direct influence on the convective velocity (Lesaffre et al., 2005).

## 3.2 The reduction in electron abundance during the explosion

The demise of an accreting white dwarf begins when the central temperature and density are such that the heating from the  $^{12}\text{C} + ^{12}\text{C}$  reaction becomes greater than the cooling from thermal neutrino emission. For a density  $\rho = 2.0 \times 10^9 \text{ g cm}^{-3}$  this requires a temperature  $T \approx 3.0 \times 10^8 \text{ K}$  (see Gasques et al., 2005, for a recent calculation). Initially the heating timescale is long,  $t_{\text{H}} \equiv T(dT/dt)^{-1} \sim 10^3 \text{ yr}$ ; as the temperature rises and the reaction rate increases,  $t_{\text{H}}$  decreases. Woosley et al. (2004) estimate that when  $T > 7.6 \times 10^8 \text{ K}$ , fluctuations in the temperature are sufficient to ensure that a local patch can run away and the flame ignites.

The basic reactions during  $^{12}\text{C}$  burning were first worked out in the context of core carbon burning in evolved stars (Reeves & Salpeter, 1959; Cameron, 1959). During simmering,  $^{12}\text{C}$  is primarily consumed via  $^{12}\text{C}(^{12}\text{C}, \alpha)^{20}\text{Ne}$  and  $^{12}\text{C}(^{12}\text{C}, p)^{23}\text{Na}$ . These reactions occur with a branching ratio 0.56/0.44 for  $T < 10^9 \text{ K}$  (Caughlan & Fowler, 1988). At temperatures below  $\approx 7 \times 10^8 \text{ K}$ , neutronization—that is, a reduction in  $Y_e$ —occurs via the reaction chain  $^{12}\text{C}(p, \gamma)^{13}\text{N}(e^-, \nu_e)^{13}\text{C}$ . This electron capture implies that there is a maximum  $Y_e$  at the time of the explosion, as first pointed out by Piro & Bildsten (2008). One can readily estimate the change in electron abundance,  $\Delta Y_e$ . For simplicity, take the branching ratio for  $^{12}\text{C} + ^{12}\text{C}$  to be 1:1 for producing  $p + ^{23}\text{Na}$  and  $^4\text{He} + ^{20}\text{Ne}$ . Thus there is one  $p$  produced for every four  $^{12}\text{C}$  consumed. Two additional  $^{12}\text{C}$  are consumed via  $^{12}\text{C}(n, \gamma)^{13}\text{C}(^4\text{He}, n)^{16}\text{O}$ , which also destroys one  $^4\text{He}$  nucleus, and via  $^{12}\text{C}(p, \gamma)^{13}\text{N}(e^-, \nu_e)^{13}\text{C}$ , which also destroys one  $p$ . Thus for every 6  $^{12}\text{C}$  consumed there is one electron capture, so that  $dY_e/dY_{12} \approx 1/6$ , where  $Y_{12}$  is the molar abundance of  $^{12}\text{C}$ . As an estimate for the heating from this reaction sequence, summing over the  $q$ -values for the strong reactions gives a net heat release of  $(16 \text{ MeV})/6 = 2.7 \text{ MeV}$  per  $^{12}\text{C}$  nucleus con-

sumed. Note that at densities above  $1.7 \times 10^9 \text{ g cm}^{-3}$ , the reaction  $^{23}\text{Na}(e^-, \nu_e)^{23}\text{Ne}$  contributes to the rate of decrease in  $Y_e$ , so that  $dY_e/dY_{12} \approx 1/3$  at those densities. The total effective rate of  $dY_e/dY_{12}$  depends on the rate of convective mixing and the size of the convective core (see § 3.3.3) but is always at least as large as the contribution from  $^{13}\text{N}(e^-, \nu_e)^{13}\text{C}$ . In the following sections, we investigate these reactions in detail.

### 3.2.1 The role of neon-22 and other trace nuclides

Reactions on  $^{22}\text{Ne}$ ,  $^{23}\text{Na}$ , and other trace nuclides also occur during shell-burning in asymptotic giant branch (AGB) stars, and we briefly summarize their role in that context before describing the very different environment in a simmering white dwarf core. In AGB stars more massive than about  $4 M_\odot$ , the hydrogen burning shell, at a temperature of 60-100 MK, extends into the convective envelope. The envelope composition is then directly affected by the various hydrogen-burning cycles: CNO, NeNa, and MgAl (Lattanzio & Boothroyd, 1997; Herwig, 2005). The hydrogen-burning shell is also disturbed by thermal pulses due to ignition of the helium layer. At each pulse, dredge-up of material may occur, in which helium-burnt material is mixed into the stellar envelope, polluting it with  $^4\text{He}$ ,  $^{12}\text{C}$ ,  $^{22}\text{Ne}$ , and heavy *s*-process elements (Izzard et al., 2007). Thus, the fate of  $^{22}\text{Ne}$  is either to contribute to hydrogen burning via  $^{22}\text{Ne}(p, \gamma)^{23}\text{Na}$  or to become a neutron source for the *s*-process via the  $^{22}\text{Ne}(\alpha, n)^{25}\text{Mg}$  reaction. The  $^{22}\text{Ne}(\alpha, n)^{25}\text{Mg}$  reaction requires the high temperatures ( $T > 2.5 \times 10^8 \text{ K}$ ) that can be found at the bottom of the pulse-driven convective zone during the helium shell flashes. The neutrons are released with high density [ $\log(N_n/\text{cm}^{-3}) \sim 10$ ] in a short burst (Gallino et al., 1998; Busso et al., 1999). These peak neutron densities are realized for only about a year, followed by a neutron density tail that lasts a few years, depending on the stellar model assumptions. These neutrons are the genesis of the classic high-temperature *s*-process in AGB stars.

Should  $^{23}\text{Na}$  be present, there are two usual possibilities for subsequent nuclear processing in AGB stars via either the  $^{23}\text{Na}(p, \alpha)^{20}\text{Ne}$  reaction or the  $^{23}\text{Na}(p, \gamma)^{24}\text{Mg}$  reaction. The former reaction gives rise to the classical NeNa cycle (Marion & Fowler, 1957; Rolfs & Rodney, 1988; Rowland et al., 2004), whereas the competing  $(p, \gamma)$  reaction transforms  $^{23}\text{Na}$  to heavier isotopes and bypasses the NeNa cycle. How much material is processed through the  $(p, \alpha)$  reaction on  $^{23}\text{Na}$  as opposed to the competing  $(p, \gamma)$  reaction is of interest for AGB star (and classical novae) nucleosynthesis. New measurements of the  $^{23}\text{Na} + p$  cross section (Rowland et al., 2004) suggest that for  $T = (20\text{--}40)$  MK  $^{23}\text{Na}(p, \gamma)^{24}\text{Mg}$  competes with the  $(p, \alpha)$  branch, disrupts the NeNa cycle, and produces a flow into the MgAl hydrogen burning cycle.

Caution about intuition developed for reaction sequences on  $^{22}\text{Ne}$  and  $^{23}\text{Na}$  in AGB star environments seems prudent when applied to the dense, carbon-rich environments of white dwarfs near the Chandrasekhar mass limit. During the slow  $^{12}\text{C}$  simmering preceding the explosion, the large  $Y_{12}$  ensures that  $p$  liberated by the  $^{12}\text{C}(^{12}\text{C}, p)^{23}\text{Na}$  branch will capture preferentially onto  $^{12}\text{C}$ , rather than  $^{22}\text{Ne}$  or  $^{23}\text{Na}$ . Figure 3.1 shows the ratio of thermally averaged cross-sections,  $\lambda \equiv N_{\text{A}} \langle \sigma v \rangle$ , to that for  $^{12}\text{C}(p, \gamma)^{13}\text{N}$  for three reactions:  $^{22}\text{Ne}(p, \gamma)^{23}\text{Na}$  (*solid line*),  $^{23}\text{Na}(p, \alpha)^{20}\text{Ne}$  (*dashed line*), and  $^{23}\text{Ne}(p, n)^{23}\text{Na}$  (*dotted line*). In addition to the Coulomb penetration, there are numerous resonances that determine how the cross-sections change with temperature. When the ratio of the thermally averaged cross-sections is of order unity, as it is for  $^{22}\text{Ne}(p, \gamma)^{23}\text{Na}$ , then the proton capture is determined by the relative abundances of  $^{22}\text{Ne}$  and  $^{12}\text{C}$ .

Note that for the latter two reactions, we plot the largest proton-consuming branch rather than the  $(p, \gamma)$  branch. We include screening in all reactions (Yakovlev et al., 2006) with the plasma taken to consist of  $^{12}\text{C}$  and  $^{16}\text{O}$  with mass fractions of 0.3 and 0.7, respectively. For  $T > 10^8$  K,  $\lambda[^{22}\text{Ne}(p, \gamma)^{23}\text{Na}]$  is well-constrained experimentally (Iliadis et al., 2001). For a white dwarf with a central density  $\rho = 2 \times 10^9$  g cm $^{-3}$

the ignition temperature (where nuclear heating dominates over cooling via thermal neutrino emission) is  $\approx 3 \times 10^8$  K (Gasques et al., 2005); the burning timescale becomes less than the timescale for  $^{23}\text{Na}(e^-, \nu_e)^{23}\text{Ne}$  once the temperature increases beyond  $T \gtrsim 6 \times 10^8$  K. Over this range, the thermally averaged cross-sections for  $^{22}\text{Ne}(p, \gamma)^{23}\text{Na}$  and  $^{12}\text{C}(p, \gamma)^{13}\text{N}$  are comparable, but the abundance of  $^{12}\text{C}$  is far greater; having  $p$  capture preferentially onto  $^{22}\text{Ne}$  would therefore require it to have a mass fraction roughly twice that of  $^{12}\text{C}$ .

At densities greater than  $1.7 \times 10^9$  g cm $^{-3}$ , the reaction  $^{23}\text{Na}(e^-, \nu_e)^{23}\text{Ne}$  produces roughly one  $^{23}\text{Ne}$  nucleus for every six  $^{12}\text{C}$  nuclei consumed. The screened, thermally averaged cross-section for  $^{23}\text{Ne}(p, n)^{23}\text{Na}$  is  $\gtrsim 30$  times that of  $^{12}\text{C}(p, \gamma)^{13}\text{N}$  (Fig. 3.1), so that  $^{23}\text{Ne}$  could become a competitive sink for protons. For our self-heating burn (see § 3.3.1) starting at  $\rho = 3 \times 10^9$  g cm $^{-3}$ , the abundance of  $^{23}\text{Ne}$  reaches  $Y_{23} = 3 \times 10^{-4}$  ( $Y_{23} \approx 0.015Y_{12}$ ) by the point the heating timescale  $\tau_{\text{H}}$  becomes shorter than the timescale for electron captures onto  $^{23}\text{Na}$ . Although our one-zone approximation overestimates the amount of  $^{12}\text{C}$  that must be consumed to raise the central temperature (see § 3.3.3), should enough of the convective core lie above the threshold for electron capture onto  $^{23}\text{Na}$ , the abundance of  $^{23}\text{Ne}$  can become large enough to choke off the  $^{12}\text{C}(p, \gamma)^{13}\text{N}$  reaction, as noted by Piro & Bildsten (2008).

### 3.2.2 The reaction $^{13}\text{N}(e^-, \nu_e)^{13}\text{C}$

As described above, the large  $^{12}\text{C}$  abundance ensures that protons produced by  $^{12}\text{C}(^{12}\text{C}, p)^{23}\text{Na}$  lead to the formation of  $\beta^+$ -unstable  $^{13}\text{N}$  via  $^{12}\text{C}(p, \gamma)^{13}\text{N}$  unless an appreciable abundance of  $^{23}\text{Na}$  or  $^{23}\text{Ne}$  can build up. At these densities, the rate for electron capture is substantially greater than the rate of  $\beta^+$ -decay for  $^{13}\text{N}$ . The electron Fermi energy is  $\approx 5.1$  MeV  $(\rho Y_e / 10^9 \text{ g cm}^{-3})^{1/3}$ , and the  $q$ -value for the  $\beta^+$  decay of  $^{13}\text{N}$  is 2.2 MeV. As a result, there are several excited states of  $^{13}\text{C}$

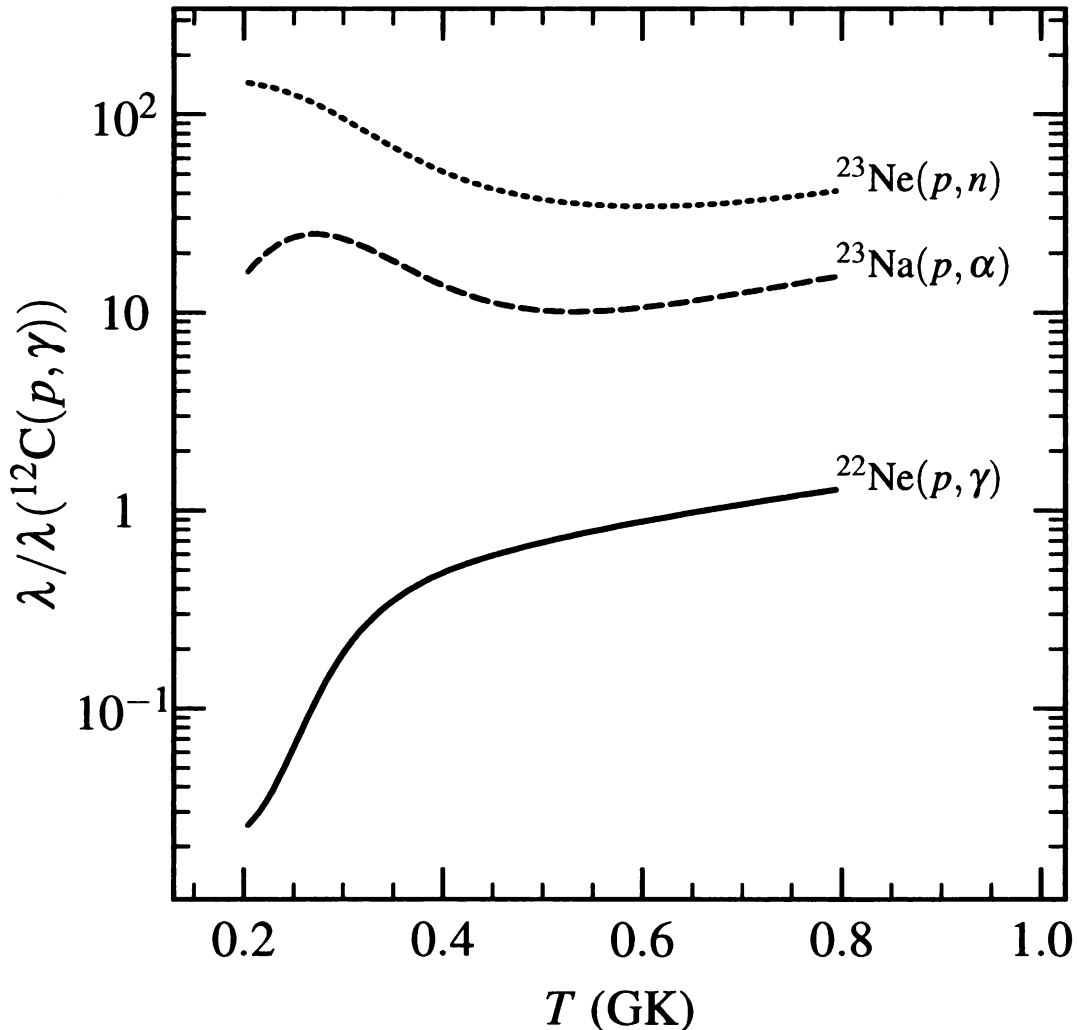


Figure 3.1: Ratio of thermally averaged cross-sections,  $\lambda \equiv N_A \langle \sigma v \rangle$ , to that for  $^{12}\text{C}(p, \gamma)$ , for three reactions:  $^{22}\text{Ne}(p, \gamma)$  (solid line);  $^{23}\text{Na}(p, \alpha)$  (dashed line); and  $^{23}\text{Ne}(p, n)$  (dotted line). Screening is included in  $\lambda$ ; we evaluate the ratio at  $\rho = 3 \times 10^9 \text{ g cm}^{-3}$  for  $^{23}\text{Ne}(p, n)$  and at  $10^9 \text{ g cm}^{-3}$  for the other two. In the temperature range where the heating timescale is slow enough for weak interactions to reduce  $Y_e$  (cf. Fig. 3.4), the thermally averaged cross-sections for  $^{22}\text{Ne}(p, \gamma)$  and  $^{12}\text{C}(p, \gamma)$  are of similar magnitude. For  $^{22}\text{Ne}$  to compete with  $^{12}\text{C}$  for  $p$ -captures at  $T \gtrsim 3 \times 10^8 \text{ K}$  requires a  $^{22}\text{Ne}$  mass fraction  $X_{22} \gtrsim (22/12)X_{12}$ . At densities less than the electron capture threshold on  $^{23}\text{Na}$  a small flow of  $^{23}\text{Na}(p, \alpha)^{20}\text{Ne}$  can occur (cf. Fig. 3.2). At higher densities  $^{23}\text{Na}$  electron captures to form  $^{23}\text{Ne}$ ; the large cross-section for  $^{23}\text{Ne}(p, n)^{23}\text{Na}$  allows it to compete with captures onto  $^{12}\text{C}$  if  $Y_{23}/Y_{12} \gtrsim 1\%$ .

into which the electron can capture. Of these, the transition to the excited state  $E_{\text{exc}} = 3.68$  MeV, with spin and parity  $J^\pi = 3/2^-$ , is an allowed Gamow-Teller transition. We computed the electron capture rate using the experimental  $\log ft$  for the ground-state transition (Ajzenberg-Selove, 1991). Gamow-Teller strengths to excited states were calculated with the shell-model code OXBASH (Brown et al., 2004) employing the Cohen-Kurath II potential (Cohen & Kurath, 1967) in the  $p$ -shell model space. A quenching factor of 0.67 (Chou et al., 1993) was applied to this strength, and the resulting  $ft$  values were used with the analytical phase space approximations of Becerril Reyes et al. (2006) to obtain the capture rate. These shell-model calculations agree well with recent ( $^3\text{He}, t$ ) scattering data (Zegers et al., 2007). At  $\rho Y_e = 10^9$  g cm $^{-3}$ , captures into the excited state at  $E_{\text{exc}} = 3.68$  MeV account for  $\gtrsim 0.3$  of the total rate ( $R_{\text{ec}} = 12$  s $^{-1}$ ); this fraction increases with density. Because  $R_{\text{ec}} > (G\bar{\rho})^{-1/2}$ , this capture does not freeze out during the simmering, unlike capture onto  $^{23}\text{Na}$ . Although the capture into the excited level does not increase the capture rate substantially beyond that for the ground-state-to-ground-state transition, it does increase the heat deposited into the white dwarf from this reaction. We find the heat deposited from this reaction, at  $\rho Y_e = 10^9$  g cm $^{-3}$ , to be 1.3 MeV.

### 3.2.3 Production and subsequent captures of neutrons

Finally, we consider the contribution from heavier nuclei, such as  $^{56}\text{Fe}$ , inherited from the main-sequence star. In AGB stars the reaction  $^{13}\text{C}(\alpha, n)^{16}\text{O}$  (during a He shell flash,  $^{22}\text{Ne}(\alpha, n)^{25}\text{Mg}$  also contributes) acts as a neutron source for the  $s$ -process. In contrast, the large  $^{12}\text{C}$  abundance of the white dwarf core prevents a strong  $s$ -process flow during the pre-explosion simmering. The cross-section for  $^{12}\text{C}(n, \gamma)^{13}\text{C}$  is 63.5 times smaller than the cross-section for  $^{56}\text{Fe}(n, \gamma)^{57}\text{Fe}$  (Bao & Kappeler, 1987) at an energy of 30 MeV, which is not sufficient to overcome the vastly larger abundance of  $^{12}\text{C}$  nuclei (for a progenitor with solar metallicity, the  $^{12}\text{C}:^{56}\text{Fe}$  ratio [for a  $^{12}\text{C}$  mass

El.	A	El.	A	El.	A	El.	A
n							
H	1-3	F	15-24	Cl	31-44	Mn	46-63
He	3-4	Ne	17-28	Ar	31-47	Fe	46-66
Li	6-8	Na	20-31	K	35-46	Co	50-67
Be	7, 9-11	Mg	20-33	Ca	35-53	Ni	50-73
B	8, 10-14	Al	22-35	Sc	40-53	Cu	56-72
C	9-16	Si	22-38	Ti	39-55	Zn	55-72
N	12-20	P	26-40	V	43-57	Ga	60-75
O	13-20	S	27-42	Cr	43-60	Ge	59-76

Table 3.1: 430-Nuclide Reaction Network

fraction of 0.3] is 1400:1).

### 3.3 Reaction network calculations

In this section we investigate the reactions that occur during simmering in more detail using a “self-heating” reaction network. Under isobaric conditions the temperature  $T$  evolves with time according to

$$\frac{dT}{dt} = \frac{\varepsilon}{C_P}. \quad (3.1)$$

Here  $C_P$  is the specific heat at constant pressure, and the heating rate  $\varepsilon$  is given by equation (2.11). The neutrino loss rate, per unit mass, from the weak reactions is taken from Fuller et al. (1982) and Langanke & Martínez-Pinedo (2001). We neglect thermal neutrino emission processes; this is an excellent approximation over most of the integration. Our reaction network incorporated 430 nuclides up to  $^{76}\text{Ge}$  (see Table 3.1). We use the reaction rates from the library REACLIB (Rauscher & Thielemann, 2000; Sakharuk et al., 2006, and references therein). We incorporated screening using the formalism of Graboske et al. (1973). The matter does not reach nuclear statistical equilibrium or quasi-nuclear statistical equilibrium. Thus, although our treatment of

screening does not preserve detailed balance (Calder et al., 2007) this does not affect our calculation. Our equation of state has contributions from electrons, radiation, and strongly coupled ions. We include thermal transport by both degenerate electrons and photons (for a complete description of our thermal routines, see Brown et al. 2002, and references therein). At conditions of  $\rho = (1-3) \times 10^9 \text{ g cm}^{-3}$  and  $T = 5 \times 10^8 \text{ K}$ , the specific heat  $C_P$  is dominated by the ions, which are in a liquid state (plasma parameter  $\Gamma \equiv \langle Z^{5/3} \rangle (e^2/k_B T) (\rho Y_e N_A)^{1/3} \approx 10$ ), and have  $C_P \approx 2.9 k_B N_A / \langle A \rangle$ , where  $\langle A \rangle$  is the average atomic mass.

### 3.3.1 The reactive flows

In this section we refine our estimate of  $dY_e/dY_{12}$  made in § 3.2.2. We integrate equation (3.1) starting from the temperature at which heating from the  $^{12}\text{C} + ^{12}\text{C}$  reaction equals the heat loss from thermal neutrino losses (this determines the onset of thermal instability). For simplicity, we split the solution of the thermal and network equations. That is, for each time-step  $dt$  we solve the thermal equations to obtain  $T$  and  $\rho$ , integrate the reaction network at that  $T$  and  $\rho$  to compute  $Y_i$  and  $\varepsilon$ , and use  $\varepsilon$  to advance the solution of equation (4.1).

In the initial phases of the simmering, the convective timescale is slow, and our one-zone calculations give an adequate description of the heating (when corrected for the gradient in temperature). As the temperature of the white dwarf increases, the heating timescale  $t_H$  decreases; moreover, the convective mixing becomes more rapid, and one must treat the hydrodynamical flows in order to calculate the nucleosynthesis properly (see § 3.3.3). In this section, we will restrict our integration to where  $T < 0.6 \text{ GK}$ , for which the heating timescale is  $\gtrsim 10^4 \text{ s}$ , so that electron captures onto  $^{23}\text{Na}$  are not frozen out.

To explore the reaction channels that link  $^{12}\text{C}$  consumption with the reduction in

$Y_e$ , we define the reactive flow between nuclides  $i$  and  $j$  as

$$F(i \rightarrow j) \equiv \int_t \left| \frac{dY_i}{dt} \right|_{i \rightarrow j} dt, \quad (3.2)$$

where the integral is for the reactions linking nuclide  $i$  with  $j$ . We differentiate between  $F(i \rightarrow j)$  and  $F(j \rightarrow i)$ , i.e., we treat inverse rates separately. Figures 3.2 and 3.3 show the reactive flows for  $\rho = 10^9 \text{ g cm}^{-3}$  and  $3 \times 10^9 \text{ g cm}^{-3}$ , respectively. In both cases the composition is  $\{X_{12}, X_{16}, X_{22}\} = \{0.3, 0.7, 0.0\}$ . Each row of the chart is a different element ( $Z$ ), with the columns corresponding to neutron number. For viewing ease, we only plot those flows having  $F > 0.01 \cdot \max(F)$ , and we indicate the strength of the flow by the line thickness. We highlight the flows of the initial  $^{12}\text{C}$  fusion reactions in red. For illustrative purposes, we only show the flows for when the temperature is not sufficiently hot for photodissociation of  $^{13}\text{N}$ . Finally, by convention and to avoid cluttering the plot, we do not show flows into or out of  $p$ ,  $n$ , and  $^4\text{He}$ .

To facilitate comparisons between different runs, we define a normalized flow as

$$\tilde{F}(i \rightarrow j) \equiv \frac{F(i \rightarrow j)}{F(^{12}\text{C} \rightarrow ^{23}\text{Na}) + F(^{12}\text{C} \rightarrow ^{20}\text{Ne})}. \quad (3.3)$$

At a density of  $10^9 \text{ g cm}^{-3}$  we find  $\tilde{F}(^{12}\text{C} \rightarrow ^{23}\text{Na}) = 0.43$  and  $\tilde{F}(^{12}\text{C} \rightarrow ^{20}\text{Ne}) = 0.57$ , which reflects the branching ratio (Caughlan & Fowler, 1988). In agreement with the arguments in § 3.2, most of the protons liberated by  $^{12}\text{C}(^{12}\text{C}, p)^{23}\text{Na}$  capture onto  $^{12}\text{C}$ , with  $\tilde{F}(^{12}\text{C} \rightarrow ^{13}\text{N}) \approx \tilde{F}(^{13}\text{N} \rightarrow ^{13}\text{C}) = 0.20$ . Note that if all  $p$  were to capture onto  $^{12}\text{C}$ , we would have  $\tilde{F}(^{12}\text{C} \rightarrow ^{13}\text{N})/\tilde{F}(^{12}\text{C} \rightarrow ^{23}\text{Na}) = 0.5$ , because the reaction  $^{12}\text{C}(^{12}\text{C}, p)^{23}\text{Na}$  consumes two  $^{12}\text{C}$ . The  $\alpha$ -particle released by the  $^{12}\text{C}(^{12}\text{C}, \alpha)^{20}\text{Ne}$  reaction captures onto  $^{13}\text{C}$  to form  $^{16}\text{O}$  and a neutron, which in turn destroys another  $^{12}\text{C}$  via  $^{12}\text{C}(n, \gamma)^{13}\text{C}$ . The flow  $\tilde{F}(^{12}\text{C} \rightarrow ^{13}\text{C}) = 0.26$  and nearly matches the number

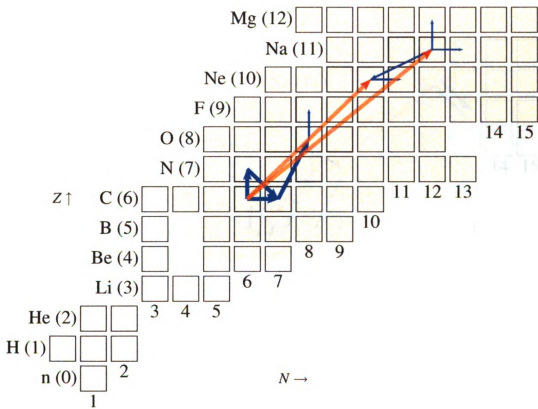


Figure 3.2: Flows during a constant-pressure self-heating burn at  $\rho = 10^9 \text{ g cm}^{-3}$  with an initial composition  $\{X_{12}, X_{16}, X_{22}\} = \{0.3, 0.7, 0.0\}$ . We integrate over the period of the burn with  $T < 6 \times 10^8 \text{ K}$ . Each row contains the isotopes of a particular element  $Z$ , with the columns containing different neutron numbers  $N$ . The width of the arrow is proportional to the magnitude of the flow, with only those flows having magnitude  $> 0.01 \cdot \max(F)$  being shown. The primary  $^{12}\text{C} + ^{12}\text{C}$  reactive flows are indicated with a lighter shading and are in red.

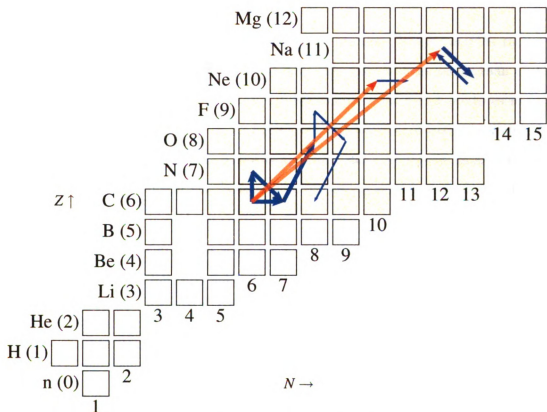


Figure 3.3: Same as in Fig. 3.2, but at  $\rho = 3 \times 10^9 \text{ g cm}^{-3}$ . The reaction  $^{23}\text{Na}(e^-, \nu_e)^{23}\text{Ne}$  is now the dominant destroyer of  $^{23}\text{Na}$  instead of  $(p, \gamma)$ ,  $(p, \alpha)$ , and  $(n, \gamma)$  reactions.

of  $\alpha$ -particles produced by  $^{12}\text{C}(^{12}\text{C}, \alpha)^{20}\text{Ne}$ ;  $n$ -captures onto  $^{23}\text{Na}$  and  $^{20}\text{Ne}$  account for the difference. At  $\rho = 10^9 \text{ g cm}^{-3}$  the only electron captures are onto  $^{13}\text{N}$ , so  $\Delta Y_e = -\tilde{F}(^{13}\text{N} \rightarrow ^{13}\text{C})$ . Dividing by  $\Delta Y_{12} = -[\tilde{F}(^{12}\text{C} \rightarrow ^{23}\text{Na}) + \tilde{F}(^{12}\text{C} \rightarrow ^{20}\text{Ne}) + \tilde{F}(^{12}\text{C} \rightarrow ^{13}\text{N}) + \tilde{F}(^{12}\text{C} \rightarrow ^{13}\text{C})]$  gives  $dY_e/dY_{12} = 0.14$  (Table 3.2). This is slightly less than the estimate of  $1/6$  (§ 3.2.2) because of the lower branching ratio of  $^{12}\text{C} \rightarrow ^{23}\text{Na}$ .

At  $\rho = 3 \times 10^9 \text{ g cm}^{-3}$ ,  $^{23}\text{Na}$  is consumed by the reaction  $^{23}\text{Na}(e^-, \nu_e)^{23}\text{Ne}$  rather than by  $p$ - or  $n$ -capture (cf. Figs. 3.2 and 3.3). The flow is much larger than that from  $^{13}\text{N}$ , because the reaction  $^{23}\text{Ne}(p, n)^{23}\text{Na}$  competes for  $p$  and produces more  $^{23}\text{Na}$ . Indeed,  $\tilde{F}(^{12}\text{C} \rightarrow ^{13}\text{C}) = 2.5\tilde{F}(^{12}\text{C} \rightarrow ^{13}\text{N})$  because of extra  $n$  produced by the reaction  $^{23}\text{Ne}(p, n)^{23}\text{Na}$ . There is an additional contribution from electron captures onto  $^{17}\text{F}$  produced via  $^{16}\text{O}(p, \gamma)^{17}\text{F}$ , but this flow is only about 4% of the  $^{23}\text{Na}(e^-, \nu_e)^{23}\text{Ne}$  flow. At both densities,  $^{22}\text{Ne}$  plays a small role in reducing  $Y_e$ , which we verified by comparing the flows for a burn with  $X_{22} = 0.06$  with those for a flow with  $X_{22} = 0.0$  (Fig. 3.3). We find that, for a burn starting at  $\rho = 3.0 \times 10^9 \text{ g cm}^{-3}$ ,  $\tilde{F}(^{22}\text{Ne} \rightarrow ^{23}\text{Na})/\tilde{F}(^{12}\text{C} \rightarrow ^{13}\text{N}) = 0.08$  and  $\tilde{F}(^{22}\text{Ne} \rightarrow ^{23}\text{Ne})/\tilde{F}(^{12}\text{C} \rightarrow ^{13}\text{C}) = 0.05$ . Although  $\lambda[^{22}\text{Ne}(p, \gamma)^{23}\text{Na}] \lesssim \lambda[^{12}\text{C}(p, \gamma)^{13}\text{N}]$  at  $T \lesssim 6 \times 10^8 \text{ K}$  (Fig. 3.1), the abundances are in a ratio of  $Y_{22}/Y_{12} = 0.11$ . Below the electron capture threshold for  $^{23}\text{Na}$ , the reaction  $^{22}\text{Ne}(p, \gamma)^{23}\text{Na}$  will cause a slight reduction in  $dY_e/dY_{12}$  equal to the ratio of  $\tilde{F}(^{22}\text{Ne} \rightarrow ^{23}\text{Na})$  to  $\tilde{F}(^{12}\text{C} \rightarrow ^{13}\text{N})$ .

Finally, we confirmed the lack of an s-process flow (§ 3.2.3) by performing a run with nuclides from  $^{20}\text{Ne}$  to  $^{56}\text{Fe}$  present at up to 3 times their solar abundances (Anders & Grevesse, 1989). The threshold for electron capture onto  $^{56}\text{Fe}$  is  $1.5 \times 10^9 \text{ g cm}^{-3}$ , and so at higher densities carbon ignition occurs in a more neutron-rich environment. We therefore start the calculation by artificially suppressing the strong interactions and allowing the mixture to come into  $\beta$ -equilibrium. We then turn on the strong reactions and let the runaway commence. In all cases the heavier nuclides

did not have a substantial impact on the reactive flows. The value for  $dY_e/dY_{12}$  is somewhat larger than 0.3 at densities  $\rho \geq 1.2 \times 10^9 \text{ g cm}^{-3}$ , the threshold density for  $^{25}\text{Mg}(e^-, \nu_e)^{25}\text{Na}(p, n)$ , because of the reactions  $^{24}\text{Mg}(p, \gamma)^{25}\text{Al}(e^-, \nu_e)^{25}\text{Mg}(e^-, \nu_e)^{25}\text{Na}$ . Of these two captures,  $^{25}\text{Al}$  is  $\beta^+$ -unstable, and hence the electron capture is fast enough to proceed throughout simmering; the capture onto  $^{25}\text{Mg}$  has a timescale, at  $\rho = 2 \times 10^9 \text{ g cm}^{-3}$ , of  $\approx 900 \text{ s}$  and will therefore freezeout during simmering, just as captures onto  $^{23}\text{Na}$  freezeout.

Our runs span a range of initial densities, from  $10^9 \text{ g cm}^{-3}$  (for which the electron Fermi energy is too low to induce electron captures onto  $^{23}\text{Na}$ ) to  $6 \times 10^9 \text{ g cm}^{-3}$ , which represents an extreme case for accretion onto a cold, initially massive white dwarf (Lesaffre et al., 2006). In all cases we took the initial  $^{12}\text{C}$  mass fraction to be  $X_{12} = 0.3$ . As noted above, the mass fraction of  $^{22}\text{Ne}$  would have to exceed that of  $^{12}\text{C}$  to change the nucleosynthesis during simmering appreciably. At higher densities,  $p$ -captures onto  $^{24}\text{Mg}$  can also play a role (§ 3.3.1), but our results will not change appreciably so long as  $X_{12}$  is not substantially less than 0.3.

The calculations, being a single reaction network integration, do not incorporate the effects of mixing in the white dwarf core. Our focus here is to elucidate the reactions that set  $Y_e$ . These calculations do not determine the total amount of carbon consumed (although see § 3.3.3 for an estimate) or the total mass of processed material that lies at a density greater than the electron capture threshold. We list our one-zone results in terms of the change in electron abundance per carbon consumed,  $dY_e/dY_{12}$ . Table 3.2 summarizes our numerical findings of  $dY_e/dY_{12}$  for densities  $10^9$ ,  $3 \times 10^9$ , and  $6 \times 10^9 \text{ g cm}^{-3}$ , for  $^{22}\text{Ne}$  mass fractions  $X_{22} = 0$  and 0.06, and finally a run (denoted as  $3Z_{sun}$  in Table 3.2) with elements heavier than  $^{20}\text{Ne}$  present at 3 times solar abundance. We use this value of  $3Z_{sun}$  as representing a rough upper limit based on the  $\approx 0.5$  dex scatter in  $[\text{Fe}/\text{H}]$  present in local field stars (Feltzing et al., 2001).

composition	density $10^9 \text{ g cm}^{-3}$	$dY_e/dY_{12}$	$\sum_i dY_i/dY_{12}$
$X_{22} = 0.00$	1.0	0.136	0.340
...	3.0	0.297	0.340
...	6.0	0.302	0.342
$X_{22} = 0.06$	1.0	0.125	0.347
...	3.0	0.301	0.344
...	6.0	0.305	0.346
$3Z_{\odot}$	1.0	0.130	0.361
...	3.0	0.349	0.370
...	6.0	0.355	0.380

Table 3.2: Change in electron abundance per carbon consumed during the pre-explosion convective burning

### 3.3.2 The effective $Q$ -value of the $^{12}\text{C} + ^{12}\text{C}$ reaction

The scope of this work is to elucidate the nuclear reactions that occur during the pre-explosion simmering, and including their effects in large-scale hydrodynamics simulations of the entire white dwarf is advisable. As an aid to such simulations, we present fits for the carbon depletion rate and effective heat deposition, which improve on previous expressions (Woosley et al., 2004). Since the reaction chain is controlled by the reaction  $^{12}\text{C} + ^{12}\text{C}$ , we write the rate of carbon consumption,  $dY_{12}/dt$  as being proportional to the thermally averaged cross-section,  $\lambda = N_{\text{A}} \langle \sigma v \rangle$

$$\frac{dY_{12}}{dt} = -M_{12} \left( \frac{1}{2} Y_{12}^2 \rho \lambda \right). \quad (3.4)$$

This definition is such that the quantity in parenthesis is the reaction rate per pair of  $^{12}\text{C}$  nuclei and  $M_{12} = 2$  if the only  $^{12}\text{C}$ -destroying reaction present is  $^{12}\text{C} + ^{12}\text{C}$ . One can determine  $M_{12}$  from summing the normalized reaction flows (eq. [3.3]) out of  $^{12}\text{C}$ .

In a similar fashion, we can define the effective heat evolved,  $q_{\text{eff}}$ , per reaction

$^{12}\text{C} + ^{12}\text{C}$  by the equation

$$\varepsilon = q_{\text{eff}} N_{\text{A}} \left( \frac{1}{2} Y_{12}^2 \rho \lambda \right). \quad (3.5)$$

With this definition, one has  $\varepsilon = (q_{\text{eff}} N_{\text{A}} / M_{12}) \times dY_{12}/dt$ ; this may be compared with equation (2.11) to relate  $q_{\text{eff}}$  to the binding energy of the nuclei. To compute these quantities, we integrated the reaction network over a grid of  $\rho$  and  $T$ , both of which were held fixed for each run. We found in all cases that the instantaneous energy generation rate  $\varepsilon$  would, after some initial transient fluctuations, settle onto a constant value until a significant ( $> 10\%$ ) depletion in  $^{12}\text{C}$  had occurred. We used this plateau in  $\varepsilon$  to obtain  $q_{\text{eff}}$  and  $M_{12}$ . For the densities of interest, the values of both  $q_{\text{eff}}$  and  $M_{12}$  obtained this way are nearly independent of temperature. We find  $M_{12} = 2.93$ ; this value is accurate to within 2% over all our runs. The value of  $q_{\text{eff}}$  increases slightly with density, but is nearly constant over the temperature range of interest. We find that  $q_{\text{eff}} = 8.91$  MeV, 9.11 MeV, and 9.43 MeV for  $\rho = 10^9$  g cm $^{-3}$ ,  $2 \times 10^9$  g cm $^{-3}$ , and  $3 \times 10^9$  g cm $^{-3}$ , respectively. At each of these densities, the quoted value of  $q_{\text{eff}}$  is accurate to within 3% over the temperature range of  $3 \times 10^8$  K to  $7 \times 10^8$  K.

For use in large-scale hydrodynamic models, one first computes the screened thermally averaged cross-section  $\lambda$  (for the most recent rate, see Gasques et al., 2005) at the thermodynamic conditions of a given cell. Combining  $\lambda$  and the cell's carbon abundance  $Y_{12}$  with our estimates of  $M_{12}$  and  $q_{\text{eff}}$ , one computes  $dY_{12}/dt$  and  $\varepsilon$  from equations (3.4) and (3.5). In effect, this procedure incorporates the results of a large reaction network and careful treatment of the detailed nuclear physics into simple expressions. We caution that these fits were obtained in the regime  $-\Delta Y_{12} < 0.003$ , for which proton captures onto  $^{23}\text{Na}$  are not competitive with proton captures onto  $^{12}\text{C}$ . Note that the heat released per  $^{12}\text{C}$  nucleus consumed is  $q_{\text{eff}}/M_{12} \approx 3.1$  MeV,

slightly higher than our simple estimate (§ 3.2), and also somewhat higher than those used by Piro & Bildsten (2008). This is because of our inclusion of heating from the  $^{13}\text{N}(e^-, \nu_e)^{13}\text{C}$  and  $^{23}\text{Na}(e^-, \nu_e)^{23}\text{Ne}$  reactions. Our estimate of the heat evolved is less than that computed under the assumption that the products of  $^{12}\text{C}$  burning are a 3:1  $^{20}\text{Ne}:^{24}\text{Mg}$  mixture (see, e.g. Woosley et al., 2004), which releases 5.0 MeV per  $^{12}\text{C}$  nucleus consumed.<sup>1</sup> Our net heating rate, per  $^{12}\text{C} + ^{12}\text{C}$  reaction, is about 10% less than that used by Woosley et al. (2004), but we effectively consume  $\approx 3$   $^{12}\text{C}$  nuclei per reaction.

The change in electron abundance is related to  $\lambda$  via

$$\frac{dY_e}{dt} = - \left( M_{12} \frac{dY_e}{dY_{12}} \right) \times \left( \frac{1}{2} Y_{12}^2 \rho \lambda \right), \quad (3.6)$$

where  $dY_e/dY_{12}$  is taken from Table 3.2. Finally, we may compute the change in the mean atomic mass,  $\langle A \rangle$ , as a function of carbon consumed. On differentiating  $\langle A \rangle = (\sum_i dY_i/dY_{12})^{-1}$ , and substituting equation 3.4, we have

$$\frac{d\langle A \rangle}{dt} = \langle A \rangle^2 M_{12} \left( \frac{1}{2} Y_{12}^2 \rho \lambda \right) \left( \sum_i \frac{dY_i}{dY_{12}} \right), \quad (3.7)$$

where the quantity  $\sum_i dY_i/dY_{12}$  is computed from the flows (eq. [3.3]) and is listed in Table 3.2. From the simple description of the reactions (§ 3.2; see also Piro & Bildsten 2008) we have, for every six  $^{12}\text{C}$  destroyed, one each of  $^{13}\text{C}$ ,  $^{16}\text{O}$ ,  $^{20}\text{Ne}$ , and  $^{23}\text{Na}$  (or  $^{23}\text{Ne}$ ), so that  $\sum_i dY_i/dY_{12} \approx$  one third. This results in a smaller change in  $\langle A \rangle$  than would result from burning  $^{12}\text{C} + ^{12}\text{C}$  to a 3:1  $^{20}\text{Ne}:^{23}\text{Na}$  mixture (in that case,  $\sum_i dY_i/dY_{12} = 0.42$ ). We advocate using equations (3.4)–(3.7) and the computed values (Table 3.2) of  $dY_e/dY_{12}$  and  $\sum_i dY_i/dY_{12}$  in numerical simulations of simmering.

---

<sup>1</sup>Note that in eq. (1) of Woosley et al. (2004), the factor of one half is subsumed into their quantity  $\lambda_{12,12}$ .

### 3.3.3 Heating of the white dwarf core and the end of simmering

In previous sections, we evaluated the heating and neutronization of the white dwarf core in terms of the rate of  $^{12}\text{C}$  consumption. We now estimate the net amount of  $^{12}\text{C}$  that is consumed in raising the white dwarf temperature and evaluate the temperature at which electron captures onto  $^{23}\text{Na}$  freeze out. In the one-zone isobaric calculations, using equations (3.4) and (3.5), we have  $dT/dY_{12} = (q_{\text{eff}}N_{\text{A}})/(M_{12}C_P)$ , so that  $\Delta T \approx 0.15 \text{ GK} (\Delta X_{12}/0.01)$ , where  $\Delta X_{12}$  is the change in mass fraction of  $^{12}\text{C}$ . The change of  $^{12}\text{C}$  abundance required to raise the temperature from  $3 \times 10^8 \text{ K}$  to  $8 \times 10^8 \text{ K}$  is then  $|\Delta Y_{12}| \approx 2.8 \times 10^{-3}$ . This is about 11% of the available  $^{12}\text{C}$ , for an initial  $^{12}\text{C}$  mass fraction of  $X_{12} = 0.3$ . Figure 3.4 shows the decrement of the  $e^-$  abundance,  $Y_e(t=0) - Y_e(t) = -\Delta Y_e$  as a function of  $^{12}\text{C}$  consumed,  $Y_{12}(t=0) - Y_{12}(t) = -\Delta Y_{12}$ . Note that we are plotting the decrement in abundance. The calculation was started at an initial density and temperature of  $\rho = 3.0 \times 10^9 \text{ g cm}^{-3}$  and  $T = 1.9 \times 10^8 \text{ K}$ . As  $t_{\text{H}}$  shortens, the electron captures onto  $^{23}\text{Na}$  “freeze out” and  $dY_e/dY_{12}$  decreases to  $\approx 1/6$ . When  $-\Delta Y_{12} \gtrsim 0.003$ , the abundances of  $^{23}\text{Na}$  and  $^{23}\text{Ne}$  have increased sufficiently that they compete with  $^{12}\text{C}$  to consume protons, and thereby halt the neutronization, in agreement with Piro & Bildsten (2008).

As noted by Piro & Bildsten (2008), a one-zone model will overestimate the heat required to raise the central temperature by a given amount, and hence overestimate the amount of  $^{12}\text{C}$  that must be consumed during simmering. We perform a calculation similar to theirs: starting with an isothermal white dwarf with a given central density and with a temperature set by equating heating from the  $^{12}\text{C} + ^{12}\text{C}$  reaction with neutrino losses, we then raise the central temperature to  $8 \times 10^8 \text{ K}$ , keeping the total white dwarf mass fixed, and follow an adiabatic temperature gradient until we intersect the original isotherm at radius  $r_{\text{conv}}$ , which we then follow to the stellar sur-

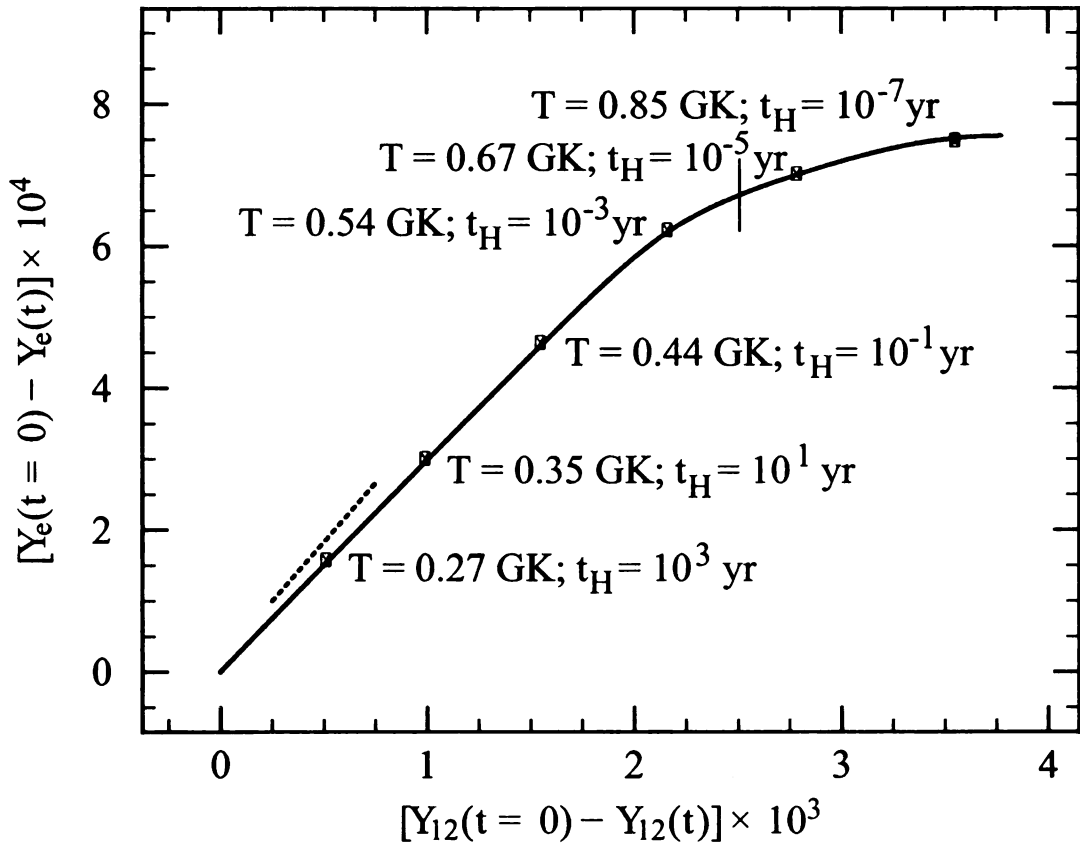


Figure 3.4: Change in electron abundance,  $Y_e(t=0) - Y_e(t)$ , as a function of carbon consumed,  $Y_{12}(t=0) - Y_{12}(t)$ . The break in the slope, at  $Y_{12}(0) - Y_{12} \approx 2 \times 10^{-3}$ , occurs when the heating timescale  $t_H = C_P/\epsilon$  becomes less than the timescale for electron capture onto  $^{23}\text{Na}$ , which is  $\approx 2700$  s at  $\rho = 3.0 \times 10^9$  g cm $^{-3}$ . We indicate this point with the thin vertical line. To guide the eye, the short dotted line indicates a slope of 1/3.

face. We compute the total stellar energy, gravitational and thermal, in both cases, and take the difference to find the heat required to raise the central temperature of the star to  $8 \times 10^8$  K. The temperature of  $8 \times 10^8$  K is chosen as a fiducial temperature representing the point at which the heating of a fluid element proceeds faster than the convective timescale (Woosley et al., 2004). The evolution of the white dwarf core is not exactly isobaric: the expanding convective zone heats the white dwarf. As the entropy of the white dwarf increases, it expands and reduces the core pressure. For an initial central density  $\rho_{\text{init}} = 3.0 \times 10^9 \text{ g cm}^{-3}$ , we find that in raising the central temperature from  $3 \times 10^8$  K to  $8 \times 10^8$  K the radius expands by a factor of 1.1 and the central pressure decreases to 0.59 of its initial value.

For initial central densities  $\rho_{\text{init}} = 10^9 \text{ g cm}^{-3}$ ,  $3 \times 10^9 \text{ g cm}^{-3}$ , and  $6 \times 10^9 \text{ g cm}^{-3}$ , corresponding to white dwarf masses of  $1.35 M_{\odot}$ ,  $1.38 M_{\odot}$ , and  $1.39 M_{\odot}$ , the initial temperatures defined by the onset of thermal instability are  $3.8 \times 10^8$  K,  $1.9 \times 10^8$  K, and  $1.0 \times 10^8$  K, respectively. The energy required to raise the central temperature to  $8 \times 10^8$  K is  $E_c = 2.11, 4.12, \text{ and } 5.58$  keV per nucleon, respectively. When the central temperature has reached  $8 \times 10^8$  K, the masses of the convective zone for these three cases are  $0.69 M_{\odot}$ ,  $1.10 M_{\odot}$ , and  $1.29 M_{\odot}$ , respectively. The spatial extent of the convective zone,  $r_{\text{conv}} \approx 1000$  km for the three cases, is in agreement with the findings of Kuhlen et al. (2006). We checked our computation of  $E_c$  by computing  $E'_c = \int_{\text{conv.}} C_P [T_{\text{final}} - T_{\text{initial}}] dM$ , as was done by Piro & Bildsten (2008). Both methods give comparable estimates, but  $E'_c$  slightly underestimates the change in energy (by  $\approx 10\%$ ), because it does not account for the expansion of the white dwarf. Neglecting the change in  $Y_e$  as the white dwarf heats introduces a small correction to  $E_c$ : for an adiabatic  $1.38 M_{\odot}$  white dwarf with a central temperature of  $8 \times 10^8$  K, a reduction in  $Y_e$  by  $1.66 \times 10^{-3}$  reduces  $E_c$  by only 3.3%.

If the white dwarf were entirely mixed, raising the central temperature  $8 \times 10^8$  K would require, for the three  $\rho_{\text{init}}$  cases here, that  $|\Delta Y_{12}| = 1.36 \times 10^{-3}, 1.66 \times 10^{-3},$

and  $1.87 \times 10^{-3}$ , respectively. Because the changes in composition are only mixed over the convective zone, the decrement in  $Y_{12}$ , and hence  $Y_e$ , is more pronounced there. Using our estimate of  $r_{\text{conv}}$ , we estimate that within the convective zone  $|\Delta Y_{12}| = 3.0 \times 10^{-3}$ ,  $2.1 \times 10^{-3}$ , and  $2.01 \times 10^{-3}$ , respectively, for  $\rho_{\text{init}}/(10^9 \text{ g cm}^{-3}) = 1.0$ , 3.0, and 6.0. Should the radial extent of the convective zone be smaller than our estimate, for example because of convective Urca losses (Stein et al., 1999; Stein & Wheeler, 2006; Lesaffre et al., 2005), the abundance of  $^{12}\text{C}$  will be further reduced in the white dwarf core. A lower  $^{12}\text{C}$  abundance reduces the laminar speed of the flame launched at the end of simmering (Timmes & Woosley, 1992; Chamulak et al., 2007).

Finally, we estimate at what point the convective mixing timescale becomes shorter than the timescale for electron captures onto  $^{23}\text{Na}$ . Using our adiabatic temperature-gradient white dwarf models, we compute the typical convective velocity  $v_{\text{rms}}$ , and hence a characteristic turnover time  $t_{\text{conv}} = r_{\text{conv}}/v_{\text{rms}}$ , using the mixing length formalism (see the discussion in Woosley et al. 2004) with the total luminosity and evaluating thermodynamical quantities at their central values. Figure 3.5 shows  $t_{\text{conv}}$  (*thick lines*) for the three cases of  $\rho_{\text{init}}$  considered above, as well as the electron capture timescale,  $t_{\text{ec}}$  for  $^{23}\text{Na}$  (*thin lines*) for those cases with a density above threshold. To estimate the effect of the  $^{23}\text{Na}/^{23}\text{Ne}$  pairs on the convective zone, we evaluated the mass fraction of these pairs for the case  $\rho_{\text{init}} = 3.0 \times 10^9 \text{ g cm}^{-3}$  when the temperature had risen to  $T = 3.5 \times 10^8 \text{ K}$  and  $t_{\text{ec}} \approx t_{\text{conv}}$  (Fig. 3.5, *solid line*). At this point the convective core has a mass  $0.5 M_{\odot}$  which is comparable to their calculation. We estimate, from the energy required to heat the white dwarf to this point, that the mass fraction of  $^{23}\text{Na}/^{23}\text{Ne}$  pairs in the convective zone will be  $X_{23} = 0.004$  at this time. We note that such a large number of Urca pairs will have a dramatic effect on the properties of the convection zone (Lesaffre et al., 2005). As is evident from Figure 3.5, there is a range of temperatures for which  $t_{\text{conv}} < t_{\text{ec}} < t_{\text{H}}$ . In this region, the effective  $dY_e/dY_{12}$  will depend on the fraction of mass with densities

above the capture threshold and on the effects of Urca losses on the convective flows, but will still be larger than the minimum value set by  $^{13}\text{N}(e^-, \nu_e)^{13}\text{C}$ . Incorporating the effects of the neutrino luminosity from the  $^{23}\text{Na}/^{23}\text{Ne}$  reactions in this regime is numerically challenging (Lesaffre et al., 2005, 2006) and beyond the scope of this work; for now, we just note that this is the primary uncertainty in determining the amount of  $^{12}\text{C}$  consumed during the pre-explosive phase, and a better treatment is needed.

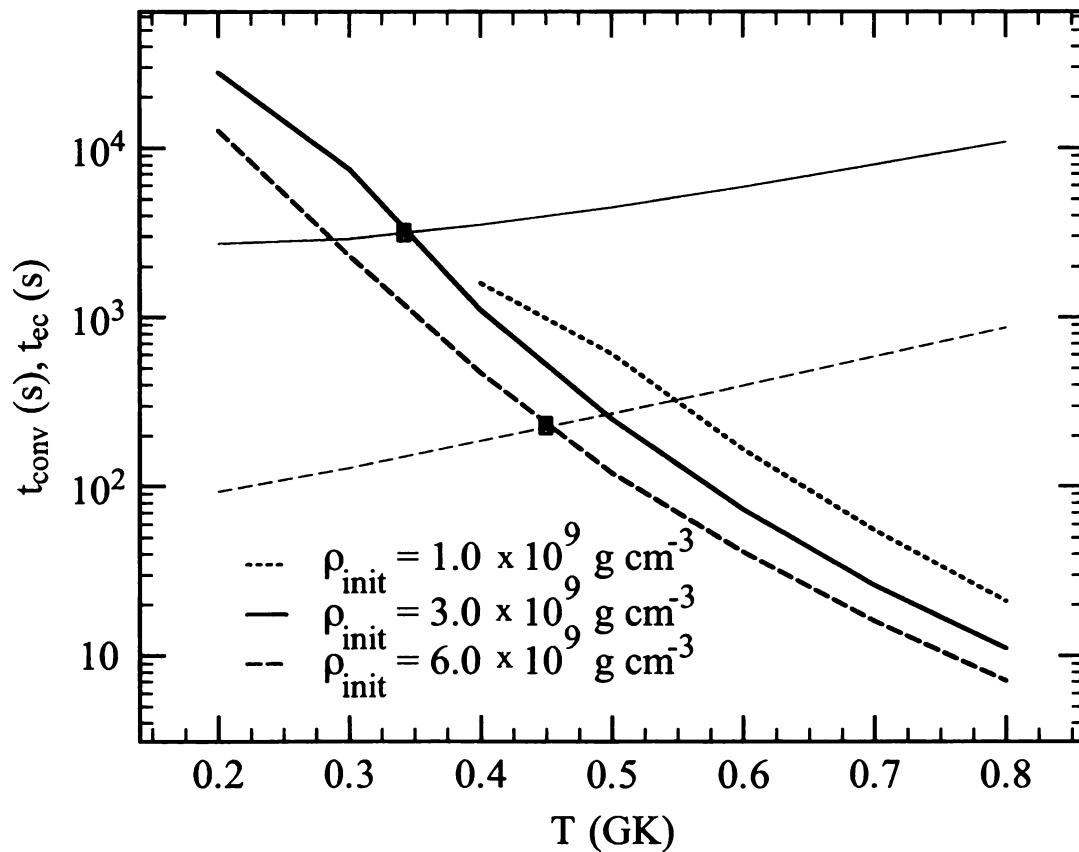


Figure 3.5: Mixing length convective timescales (*thick lines*) and electron capture timescales (for densities above threshold) for  $^{23}\text{Na}$  (*thin lines*), as a function of the central temperature during the simmering. Three initial densities are shown:  $10^9 \text{ g cm}^{-3}$  (*dotted line*),  $3 \times 10^9 \text{ g cm}^{-3}$  (*solid lines*), and  $6 \times 10^9 \text{ g cm}^{-3}$  (*dashed lines*). The electron capture timescales increase as the white dwarf heats because the density decreases during simmering.

### 3.4 Discussion and conclusions

Using a nuclear reaction network coupled to the equation for self-heating at constant pressure (eq. [3.1]), we have investigated the change in  $Y_e$  induced by electron captures on nuclei produced by  $^{12}\text{C}$  fusion during the pre-explosion simmering of the white dwarf. We confirm that there is a maximum  $Y_e$  at flame ignition (Piro & Bildsten, 2008). We quantified the role of  $^{22}\text{Ne}$  and other trace nuclides in setting the change in electron abundance with  $^{12}\text{C}$  consumption by using a full reaction network, and we included the heating from electron captures into an excited state of  $^{13}\text{C}$ . We gave simple formulae (eq. [3.4]–[3.7]) for the energy generation rate, the rate of change in electron abundance, and the rate of change in the mean atomic mass to include the detailed nuclear physics into large-scale hydrodynamical simulations.

Our estimates of the maximum  $Y_e$  at the time of the explosion are roughly similar to those of Piro & Bildsten (2008). If we neglect the effect of thermal neutrino losses on the evolution of the white dwarf, then  $Y_e$  is reduced by  $2.7 \times 10^{-4}$ – $6.3 \times 10^{-4}$  within the convective zone. This reduction in  $Y_e$  depends predominantly on the amount of  $^{12}\text{C}$  consumed prior to ignition. The electron captures during simmering reduce  $Y_e$  below the value set by neutron-rich  $^{22}\text{Ne}$  inherited from core He burning by the white dwarf’s progenitor star. Reducing  $Y_e$  in the explosion depresses the yield of  $^{56}\text{Ni}$  and increases the amount of  $^{54}\text{Fe}$  and  $^{58}\text{Ni}$  synthesized (Iwamoto et al., 1999; Timmes et al., 2003), even in the absence of further electron captures onto the Fe-peak isotopes in nuclear statistical equilibrium (NSE) in the densest portion of the white dwarf. As a result, any correlation between host system metallicity and white dwarf peak luminosity will be weakened for  $Z \lesssim Z_{\odot}$  (for which the reduction in  $Y_e$  due to captures during simmering is greater than the change due to initial white dwarf composition).

To illustrate how the simmering electron captures affect the light curve, we recon-

construct the comparison made by Gallagher et al. (2005), who compiled a set of SNe Ia with measured  $\Delta m_{15}(B)$ , defined as the change in  $B$  over 15 days post-peak, and host galaxies with measured abundances of oxygen to hydrogen, denoted O/H. We construct an expression for  $M_{56}$ , the mass of  $^{56}\text{Ni}$  produced in the explosion, that depends on  $dY_e/dY_{12}$  (Table 3.2),  $\Delta Y_{12}$ , and the host galaxy composition (we assume that the white dwarf has the same O/H ratio as the galaxy). The trace nuclide that predominantly sets  $Y_e$  in the white dwarf is  $^{22}\text{Ne}$ , which traces the aboriginal abundance of CNO nuclei in the main-sequence star from which the white dwarf evolved. We therefore recast the linear formula for  $M_{56}$  (Timmes et al., 2003) in terms of O/H. For simplicity, we fix the  $^1\text{H}:^4\text{He}$  ratio, as well as the ratio of heavier elements to  $^{16}\text{O}$ , to their solar system values (Asplund et al., 2005) and neglect corrections from the change in [O/Fe] with [Fe/H] (Ramírez et al., 2007) and the increase in [N/O] with [O/H] (Liang et al., 2006). With these assumptions, the mass of  $^{56}\text{Ni}$  ejected in the explosion is

$$M_{56} = M_{56.0} \left[ 1 - 72.7 \left( \frac{\text{O}}{\text{H}} \right) + 58 \frac{dY_e}{dY_{12}} \Delta Y_{12} \right], \quad (3.8)$$

where  $M_{56.0}$  is the total mass of NSE material synthesized at densities where electron captures during the explosion are negligible,  $dY_e/dY_{12}$  is the change in electron abundance with carbon consumption given in Table 3.2, and  $-\Delta Y_{12}$  is the total amount of  $^{12}\text{C}$  consumed during the pre-explosion convective phase.

Relating this to an observable such as  $\Delta m_{15}(B)$  requires an explosion model that follows the radiation transfer. Our interest here is to isolate how  $M_{56}$  changes with the CNO abundance of the progenitor when the other parameters, such as the ejecta kinetic energy and the total mass of iron-peak nuclei, are held fixed. This is important, because the relation between light curve width and peak brightness depends on these other parameters as well (see Woosley et al., 2007, for a lucid discussion). We use the model M070103 (Woosley et al., 2007), in which the total mass of iron-peak ejecta is

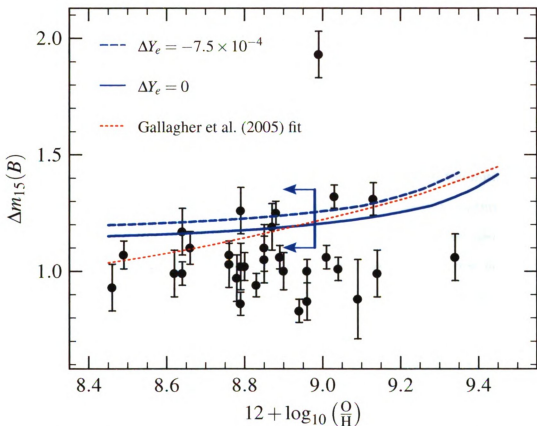


Figure 3.6: Correlation between  $12 + \log(\text{O}/\text{H})$  and  $\Delta m_{15}(B)$  induced by the electron abundance. The points in the plot are taken from Gallagher et al. (2005). We show the 'maximal' case for the reduction in  $Y_e$  during simmering (*dashed line*), in which  $dY_e/dY_{12} = 0.30$  in the early stages of the burn, which is an upper limit to the derivative. In this case  $\Delta Y_e = -7.5 \times 10^{-4}$ . For comparison, we also show the case in which there is no reduction of  $Y_e$  during simmering (*solid line*). Note that the relation between  $M_{56}$  and  $\Delta m_{15}(B)$  is shallower than that used by Gallagher et al. (2005, *dotted line*); see the text for an explanation. To the left of the vertical bar, the decrease in  $M_{56}$  due to electron captures during simmering will exceed that due to enrichment by  $^{22}\text{Ne}$ , and hence any correlation between  $\text{O}/\text{H}$  and  $\Delta m_{15}(B)$  will be masked.

0.8  $M_{\odot}$ : of that, the innermost 0.1  $M_{\odot}$  is stable iron formed *in situ* from electron captures during the explosion, with the remainder being a mix of radioactive  $^{56}\text{Ni}$  and stable Fe. Note that this model follows the peak luminosity-light curve width relation (Phillips, 1993), whereas Mazzali & Podsiadlowski (2006) suggest that varying the ratio of  $^{56}\text{Ni}$  to stable Fe may create dispersion about this relation.

Using the model of Woosley et al. (2007), we set  $M_{56.0} = 0.7 M_{\odot}$ , use equation (3.8) to compute  $M_{56}$  as a function of O/H for different  $\Delta Y_{12}$ , and interpolate from Woosley et al. (2007, Fig. 22) to find  $\Delta m_{15}(B)$ . Figure 3.6 displays this result. We plot here a maximal case (*dashed line*) with  $dY_e/dY_{12} = 0.30$  in the initial part of the simmer, appropriate for the one-zone calculation with electron captures onto  $^{23}\text{Na}$  (Fig. 3.4); for this case  $\Delta Y_e = -7.5 \times 10^{-4}$ . For comparison, we also plot a case (*solid line*) with  $\Delta Y_e = 0$  during simmering. This gives a sense of how large the variation in  $Y_e$  might be. The vertical bar indicates the value of  $12 + \log_{10}(\text{O}/\text{H})$  at which the change in  $\Delta m_{15}(B)$  from the  $^{22}\text{Ne}$  abundance equals that from the electron captures during simmering for this maximal case. To the left of this curve the linear correlation between  $^{22}\text{Ne}$  abundance and  $\Delta m_{15}(B)$  will be masked by variations in the simmering of the white dwarf. For comparison, we also show the data from the compilation of Gallagher et al. (2005) and Hamuy et al. (2000) and plot the relation between  $12 + \log(\text{O}/\text{H})$  and  $\Delta m_{15}(B)$  used by Gallagher et al. (2005, *dotted line*). This trend is much steeper than our finding. The difference is due to how the  $^{56}\text{Ni}$  mass was varied; whereas the models we use (Woosley et al., 2007) hold the kinetic energy and total mass of iron-peak ejecta fixed, Gallagher et al. (2005) based their peak brightness on delayed detonation models (Höflich et al., 2002) for which a variation in  $^{56}\text{Ni}$  also produced a change in the relative amounts of iron-peak and intermediate mass-elements, as well as a different explosion kinetic energy.

It is evident from Fig. 3.6 that the scatter in the data points is larger than the expected trend due to progenitor composition, especially at sub-solar metallicities.

Both  $\Delta Y_{12}$  and  $dY_e/dY_{12}$  depend on the central density, which is not obviously correlated with metallicity, and hence the correlation between peak brightness and O/H will be masked by differences in the pre-explosion simmering. Indeed, if the variation in  $\Delta Y_e$  were as large as the two cases we plot in Fig. 3.6, then variations in  $^{56}\text{Ni}$  would be determined more by  $\Delta Y_{12}$  than by stellar composition for galaxies with sub-solar O/H. There is a general trend that SNe Ia are systematically brighter in galaxies with active star-formation (Hamuy et al., 2000; Gallagher et al., 2005; Sullivan et al., 2006; Howell et al., 2007). Sullivan et al. (2006) showed that the SNe Ia rate increases linearly with the specific star formation rate, and that SNe Ia associated with actively star forming galaxies were intrinsically brighter than those associated with passive galaxies. Although many of these passive galaxies are more massive, and hence more metal-rich (Tremonti et al., 2004), the observed scatter in SNe Ia peak brightnesses remains much larger than the expected trend with metallicity (Piro & Bildsten, 2008; Howell et al., 2009; Gallagher et al., 2008). This suggests that the correlation with the chemical abundances of the host galaxy is a secondary effect in setting the peak brightness of SNe Ia.

# Chapter 4

## The effect of $^{22}\text{Ne}$ on flame speed

### 4.1 Introduction

The possibility that type Ia supernovae might evolve with the abundance of  $\alpha$ -elements in the host population, combined with questions about whether this introduces systematic variations in the Phillips relation, motivates further investigation of how the progenitor composition influences the explosion. As a first step, we investigate in this chapter how the abundance of  $^{22}\text{Ne}$  affects the laminar flame speed  $S_{\text{lam}}$  and width  $\delta_{\text{lam}}$  of a  $^{12}\text{C}$ - $^{16}\text{O}$ - $^{22}\text{Ne}$  mixture. Our principal conclusion is that  $S_{\text{lam}}$  increases roughly *linearly* with the  $^{22}\text{Ne}$  mass fraction  $X_{22}$ . At  $X_{22} = 0.06$ , the speedup varies, for carbon mass fraction  $X_{12} = 0.5$ , from  $\approx 30\%$  at densities  $\gtrsim 5.0 \times 10^8 \text{ g cm}^{-3}$  to  $\approx 60\%$  at lower densities.

These calculations are relevant for two regimes: 1) the initial burn near the center of the white dwarf where the gravitational acceleration is small and the laminar flame speed dominates the evolution of a bubble of ignited material (see, e.g., Zingale & Dursi, 2007), and 2) the burning at densities  $\sim 10^7 \text{ g cm}^{-3}$  where the Gibson length scale becomes  $\ell_{\text{G}} \sim \delta_{\text{lam}}$ . The Gibson scale  $\ell_{\text{G}}$  is defined by  $v(\ell_{\text{G}}) = S_{\text{lam}}$  where  $v(\ell)$  is the eddy velocity for a lengthscale  $\ell$  (see Hillebrandt & Niemeyer,

2000, for a succinct review). The region where  $\delta_{\text{lam}} = \ell_{\text{G}}$  is conjectured to be a possible location for a deflagration-to-detonation transition (Niemeyer & Woosley, 1997). Our calculation does not apply in the flamelet regime, where the buoyancy of the hot ashes generates turbulence via the Rayleigh-Taylor instability. In this regime, the effective front speed becomes independent of the laminar flame speed (Khokhlov, 1995; Reinecke et al., 1999; Zhang et al., 2006), and the composition affects the front speed only through the Atwood number,  $\text{At} \equiv (\rho_{\text{fuel}} - \rho_{\text{ash}})/(\rho_{\text{fuel}} + \rho_{\text{ash}})$ , where  $\rho_{\text{fuel(ash)}}$  is the density in the unburned (burned) material.

In § 4.2 we describe our computational method and benchmark our calculations against earlier results of Timmes & Woosley (1992). Section 4.3 presents the computed flame speeds as functions of  $\rho_{\text{fuel}}$ ,  $X_{12}$ , and  $X_{22}$ . We provide a fitted expression for  $S_{\text{lam}}$  as a function of these parameters. We also give a physical explanation for the speedup before concluding, in § 4.4, with a discussion of how the transition to distributed burning would occur at a lower density if the  $^{22}\text{Ne}$  abundance were increased.

## 4.2 The laminar flame

To solve for the conductive flame speed  $S_{\text{lam}}$ , we used the assumption of isobaric conditions to cast the equation for the energy as two coupled equations for the temperature and flux (Timmes & Woosley, 1992; Bildsten, 1995),

$$\frac{dT}{dx} = -\frac{F}{K} \tag{4.1}$$

$$\frac{dF}{dx} = \rho\varepsilon - S_{\text{lam}} \frac{\rho C_P}{K} F. \tag{4.2}$$

Here  $F$  is the heat flux and  $C_P$  is the specific heat.<sup>1</sup> The heating rate  $\varepsilon$  is given by equation (2.11) and  $d/dt = S_{\text{lam}}(d/dx)$ . Our reaction network incorporated 430 nuclides from n to  $^{76}\text{Ge}$  and is the same network used in § 3.3. We use the reaction rates from the library REACLIB (Rauscher & Thielemann, 2000; Sakharuk et al., 2006, and references therein). On the timescale of the flame passage, electron captures are unimportant, and  $Y_e$  is essentially fixed; we found that  $S_{\text{lam}}$  was unchanged when weak reactions were removed from the network, so we used only strong rates for computational efficiency. We incorporated screening using the formalism of Graboske et al. (1973). Across the flame front, the matter does not reach nuclear statistical equilibrium or quasi-nuclear statistical equilibrium until most of the  $^{12}\text{C}$  is depleted. Thus, although our treatment of screening does not preserve detailed balance (Calder et al., 2007) this does not affect our calculation of the flame speed. Our equation of state has contributions from electrons, radiation, and strongly coupled ions. We include thermal transport by both degenerate electrons and photons (for a complete description of our thermal routines, see Brown et al. 2002, and references therein).

Equations (4.1)–(4.2), when combined with appropriate boundary conditions, have  $S_{\text{lam}}$  as an eigenvalue. Ahead of the flame the material is at an arbitrary cold temperature  $T_{\text{fuel}} = 10^8 \text{K}$ ; in this region we set  $dT/dx$  to a small positive value and integrate equations (4.1)–(4.2). For simplicity, we split the solution of the thermal and network equations; that is, for each step  $dx$  we solve the thermal equations, to obtain  $T$  and  $\rho$ , integrate the reaction network at that  $T$  and  $\rho$  to compute  $Y_i$  and  $\varepsilon$ , and use that to advance the solution of the thermal equations. For our choice of  $S_{\text{lam}}$ , the second boundary condition is that  $F \rightarrow 0$  asymptotically behind the front and that  $F$  is peaked where  $\varepsilon$  is maximum. We iterated until  $S_{\text{lam}}$  had converged to within 0.01%. We find that  $S_{\text{lam}}$  is insensitive to  $T_{\text{fuel}}$  for  $\rho_{\text{fuel}} \gtrsim 5 \times 10^8 \text{ g cm}^{-3}$ .

---

<sup>1</sup>We neglect here terms such as  $\partial E/\partial X_i$ , which account for the change in the thermal properties as the abundance of nuclide  $i$  changes. These terms are much smaller than  $\varepsilon$  for matter not in NSE.

At lower densities this is no longer true, but the relative increase in  $S_{\text{lam}}$  with  $X_{22}$  remains robust.

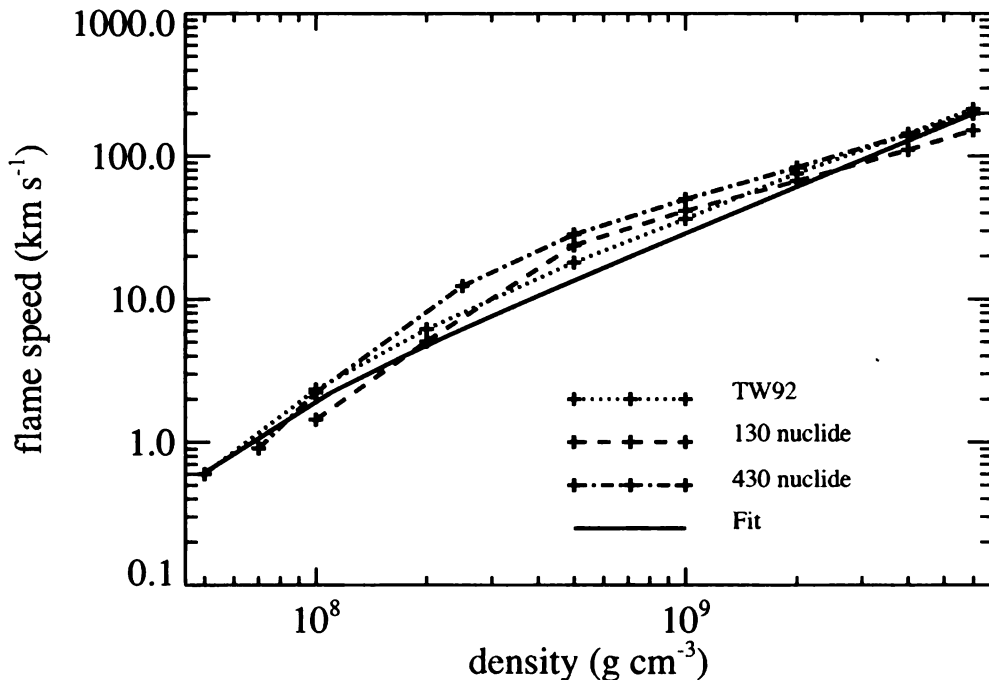


Figure 4.1: Flame speeds computed with an 130-nuclide network (*dashed line*) and a 430-nuclide network (*dash-dotted line*). We compare these with the results of Timmes & Woosley (1992, *dotted line*), and our fit (eq. [4.3]; *solid line*). Our 130-nuclide network uses the same nuclides as Timmes & Woosley (1992).

Figure 4.1 shows a comparison between our flame speeds for a 1:1 C:O mixture and those of Timmes & Woosley (1992). Here we adopt the same 130-nuclides as used in that paper. Although in this case we are using the same nuclides and starting composition, the rates, equation of state, and thermal conductivities are not identical. Overall, our flame speeds differ by no more than 25%; the largest discrepancy is at  $\rho_{\text{fuel}} = 10^8 \text{ g cm}^{-3}$ . Most of this discrepancy is due to different opacities used by the two codes. For  $\rho_{\text{fuel}} \lesssim 7 \times 10^8 \text{ g cm}^{-3}$ , photons become more efficient than electrons at transporting heat within the flame front, with the dominant opacity being free-

free. Timmes & Woosley (1992) included a fit to electron-ion scattering in the semi-degenerate regime (Iben, 1975). At these densities where  $T > 2 \times 10^9$  K and the free-free opacity dominates, the contribution from electron-ion scattering decreases the total opacity. We compared our opacities along a  $(\rho, T)$  trace generated for a run at  $\rho_{\text{fuel}} = 10^8 \text{ g cm}^{-3}$ . We found that non-degenerate electron-ion scattering can lower the opacity by  $\approx 24\%$ , depending on how the opacity is interpolated between the two limiting fits. In addition, our free-free opacities differ by 30% at the location along the  $(\rho, T)$  trace where  $|F|$  is maximum.

Finally, we also investigated the effect of reaction network size: increasing the network from 130 to 430 nuclides resulted in a 25% increase in  $S_{\text{lam}}$  at  $\rho_{\text{fuel}} = 2.0 \times 10^9 \text{ g cm}^{-3}$ ; further increases in the size of the reaction network did not yield any appreciable increases in  $S_{\text{lam}}$ .

### 4.3 Results

We now present the results of our flame calculations for different initial mixtures of  $^{12}\text{C}$ ,  $^{16}\text{O}$ , and  $^{22}\text{Ne}$  and different ambient densities. Table 4.1 lists  $S_{\text{lam}}$  and the flame width defined by  $\delta_{\text{lam}} = (T_{\text{ash}} - T_{\text{fuel}}) / \max |dT/dx|$ , with  $T_{\text{fuel(ash)}}$  being the temperature in the unburned (burned) matter. We tabulate these quantities for  $\rho_9 \equiv \rho_{\text{fuel}}/10^9 \text{ g cm}^{-3}$  ranging from 0.05 to 6.0, and  $X_{12} = 0.3\text{-}0.7$ , with the remaining composition being  $^{16}\text{O}$  and  $^{22}\text{Ne}$ . For each choice of  $\rho_9$  and  $X_{12}$ , we use 3 different  $^{22}\text{Ne}$  abundances,  $X_{22} = 0.0, 0.02, \text{ and } 0.06$ . Over most of the range in  $\rho_9$ ,  $X_{12}$ , and  $X_{22}$  in Table 4.1, we find that an increase in  $X_{22}$  from 0 to 0.06 causes  $S_{\text{lam}}$  to increase by approximately 30%. We confirmed several of the table entries using an independent diffusion equation solver that uses adaptive grids (Timmes & Woosley, 1992) and a different reaction network and opacity routine. From this, we estimate that the uncertainty in the flame speeds listed in Table 2 are  $\approx 30\%$ , with about 10%

$X_{12}$	$X_{16}$	$X_{22}$	$\rho$ ( $10^9 \text{ g cm}^{-3}$ )	$S_{\text{lam}}$ ( $\text{km s}^{-1}$ )	$\delta_{\text{lam}}$ (cm)
0.30	0.70	0.00	0.1	1.20	$1.54 \times 10^{-2}$
0.30	0.64	0.06	0.1	1.23	$1.52 \times 10^{-2}$
0.30	0.70	0.00	0.5	14.9	$5.63 \times 10^{-4}$
0.30	0.64	0.06	0.5	18.4	$4.48 \times 10^{-4}$
0.30	0.70	0.00	2.0	49.4	$7.64 \times 10^{-5}$
0.30	0.64	0.06	2.0	66.9	$5.60 \times 10^{-5}$
0.30	0.70	0.00	6.0	124	$1.88 \times 10^{-5}$
0.30	0.64	0.06	6.0	163	$1.39 \times 10^{-5}$
0.70	0.30	0.00	0.1	6.22	$3.07 \times 10^{-3}$
0.70	0.24	0.06	0.1	9.59	$1.80 \times 10^{-3}$
0.70	0.30	0.00	0.5	49.4	$1.81 \times 10^{-4}$
0.70	0.24	0.06	0.5	67.4	$1.32 \times 10^{-4}$
0.70	0.30	0.00	2.0	131	$3.00 \times 10^{-5}$
0.70	0.24	0.06	2.0	171	$2.27 \times 10^{-5}$
0.70	0.30	0.00	6.0	304	$7.93 \times 10^{-6}$
0.70	0.24	0.06	6.0	379	$6.13 \times 10^{-6}$

Table 4.1: Laminar flame speed and width

coming from numerical uncertainty and about 20% from different physics treatments as described above. We emphasize, however, that both codes find the same trends, e.g., an increase in  $S_{\text{lam}}$  with  $X_{22}$ .

We fit the tabulated  $S_{\text{lam}}$  with the approximate expression

$$\begin{aligned}
S_{\text{lam}} = & \left[ 23.26\rho_9 + 37.34\rho_9^{1.1} - 1.288 \right] \times \left[ 1 + 0.3 \left( \frac{X_{22}}{0.06} \right) \right] \\
& \times \left[ 0.3883 \left( \frac{X_{12}}{0.5} \right) + 0.09773 \left( \frac{X_{12}}{0.5} \right)^3 \right] \text{ km s}^{-1} \quad (4.3)
\end{aligned}$$

which has fit errors, as compared against speeds calculated using the 430-nuclide network with  $X_{22} = 0$ , that average 33%, with a maximum of 70%, for  $X_{12} = 0.5$  and  $\rho_9 = 0.07$ , and with a minimum of 0.1%, for  $X_{12} = 0.5$  and  $\rho_9 = 6$ . For accurate work, interpolation from Table 4.1 is preferred. At  $\rho \lesssim 10^8 \text{ g cm}^{-3}$ , the speedup is negligible for  $X_{12} = 0.3$  but increases to  $\approx 50\%$  for  $X_{12} = 0.5$ .

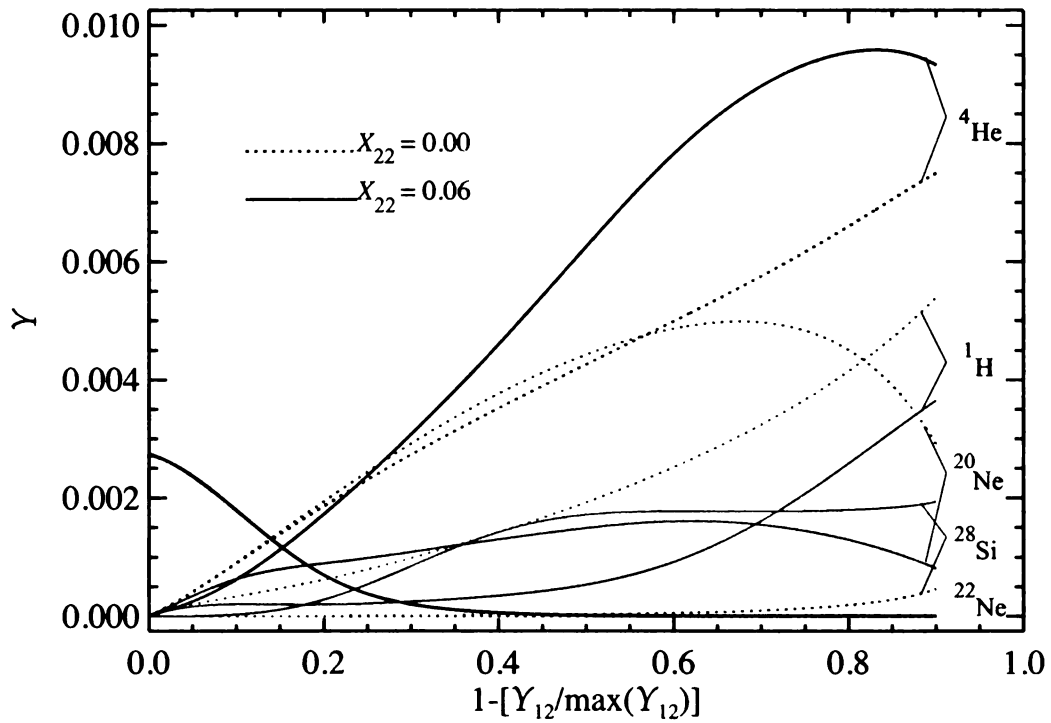


Figure 4.2: Abundances of selected nuclides during a burn at  $\rho = 2.0 \times 10^9 \text{ g cm}^{-3}$  and with an initial <sup>12</sup>C mass fraction of 0.3. We show runs with an initial <sup>22</sup>Ne abundance of 0.06 (*solid lines*) and 0.0 (*dashed lines*).

To understand how the addition of  $^{22}\text{Ne}$  increases  $S_{\text{lam}}$ , we plot in Fig. 4.2 some selected abundances  $Y = X/A$  for a flame with an initial  $X_{12} = 0.3$  and  $\rho_{\text{fuel}} = 2.0 \times 10^9 \text{ g cm}^{-3}$ . We use the fraction of  $^{12}\text{C}$  consumed,  $1 - Y_{12}/\max(Y_{12})$ , as our coordinate and plot the region where this value is monotonic with distance. In a C/O deflagration, the flame speed and width are set by the initial burning of  $^{12}\text{C}$ . The buildup of Si-group nuclides and then establishment of nuclear statistical equilibrium occur on longer timescales, so that the peak of the heat flux is reached as  $^{12}\text{C}$  is depleted via the reactions  $^{12}\text{C}(^{12}\text{C}, \alpha)^{20}\text{Ne}$  and  $^{12}\text{C}(^{12}\text{C}, p)^{23}\text{Na}(p, \alpha)^{20}\text{Ne}$ . For the case with  $X_{22} = 0.06$  (*solid lines*) one sees that  $^{22}\text{Ne}$  is depleted before the  $^{12}\text{C}$  is even half-consumed. The  $^{22}\text{Ne}$  lifetime becomes less than the  $^{12}\text{C}$  lifetime once the  $\alpha$  abundance is  $Y_4 \gtrsim 10^{-4}$ . At temperatures in the flame front the uncertainty in the  $^{22}\text{Ne}(\alpha, n)^{25}\text{Mg}$  rate is estimated to be about 10% (see Karakas et al., 2006, and references therein). This is unlike the case in AGB stars, for which the uncertainty at  $T < 3 \times 10^8 \text{ K}$  is approximately a factor of 10. Note that significant burning does not occur until the  $^{12}\text{C}$  lifetime becomes of order the time for the flame front to move one flame width. This requires temperatures in excess of  $2 \times 10^9 \text{ K}$  for the densities of interest, and so  $^{22}\text{Ne}$  is preferentially destroyed in a flame via  $(\alpha, n)$  rather than by  $p$ -capture (cf. Podsiadlowski et al., 2006).

The neutrons made available from the destruction of  $^{22}\text{Ne}$  capture preferentially onto  $^{20}\text{Ne}$  formed during  $^{12}\text{C}$  burning. At  $\rho_{\text{fuel}} \gtrsim 5 \times 10^8 \text{ g cm}^{-3}$ , successive  $(n, \alpha)$  reactions build up  $^{17}\text{O}$  and  $^{14}\text{C}$ , the latter of which then undergoes  $^{14}\text{C}(p, n)^{14}\text{N}$   $(n, \alpha)^{11}\text{B}(p, 2\alpha)^4\text{He}$ . At densities of  $\rho_{\text{fuel}} \lesssim 5 \times 10^8 \text{ g cm}^{-3}$  and carbon abundances  $X_{12} = 0.5$ , the flow  $^{20}\text{Ne}(n, \gamma)^{21}\text{Ne}(n, \alpha)^{18}\text{O}(p, \alpha)^{15}\text{N}(p, \alpha)^{12}\text{C}$  also contributes. The net effect of having  $^{22}\text{Ne}$  in the fuel mixture is that during  $^{12}\text{C}$  burning, the abundance of protons is depressed and the abundance of  $^4\text{He}$  elevated, as illustrated in Fig. 4.2. The fact that these flows require two neutron captures onto the products of  $^{12}\text{C} + ^{12}\text{C}$  suggests that the increase in  $\varepsilon$  should scale roughly as  $X_{22}^2$ . Since  $S_{\text{lam}} \propto \varepsilon^{1/2}$ , this

implies that the increase in flame speed will be linear in  $X_{22}$ , which agrees with the numerical solution of equation (4.1). Because these flows are initiated by  $n$ -capture onto  $^{20}\text{Ne}$ , we tested our sensitivity to the reaction rate by recomputing the case  $X_{12} = 0.5$  and  $\rho_{\text{fuel}} = 7.0 \times 10^7 \text{ g cm}^{-3}$ . A decrease in the  $^{20}\text{Ne} + n$  rate by a factor of 10 produced a decrease in the flame speedup, from 70% to 20%. At higher densities there was no difference in the speedup. The only case for which there was no increase in  $S_{\text{lam}}$  was for  $\rho_{\text{fuel}} \lesssim 10^8 \text{ g cm}^{-3}$  and  $X_{12} = 0.3$  (see Table 4.1). For this case, the slower consumption of  $^{22}\text{Ne}$  relative to  $^{12}\text{C}$  and  $(n, \gamma)$  captures on  $^{25}\text{Mg}$  suppress the generation of  $\alpha$ -particles early in the burn.

## 4.4 Discussion

We have computed the laminar flame speed in an initially degenerate plasma consisting of  $^{12}\text{C}$ ,  $^{16}\text{O}$ , and  $^{22}\text{Ne}$ . We find that, over a wide range of initial densities and  $^{12}\text{C}$  abundances, the flame speed increases roughly linearly with  $^{22}\text{Ne}$  abundance, with the increase being  $\approx 30\%$  for  $X_{22} = 0.06$ , although there are deviations from this rule at lower densities. These studies are relevant to the initial burning at the near-center of the white dwarf, and at late times where the flame may make a transition to distributed burning. To see how the increase in laminar flame speed changes the density where the burning becomes distributed, we write  $S_{\text{lam}} \approx \rho^\eta(1 + \xi X_{22})$  and find from our table that at  $\rho_{\text{fuel}} = 7.0 \times 10^7 \text{ g cm}^{-3}$  (the lowest density for which our numerical scheme converged) and  $X_{12} = 0.5$ ,  $\eta \approx 1.6$  and  $\xi \approx 0.7/0.06$ . Recent numerical studies (Zingale et al., 2005) find that the Rayleigh-Taylor instability drives turbulence that obeys Kolmogorov statistics, so that  $\ell_{\text{G}} \propto S_{\text{lam}}^3$ . Numerically, we find that the flame width scales roughly as  $\delta_{\text{lam}} \propto S_{\text{lam}}^{-1.5}$ , so solving for  $\delta_{\text{lam}}/\ell_{\text{G}} = 1$  implies that increasing  $X_{22}$  from 0 to 0.06 would lower the transition density by  $\approx 30\%$ . A reduction in the density of this transition will lead to a reduc-

tion in the mass of  $^{56}\text{Ni}$  synthesized (Höfllich et al., 1995). We conjecture that if a deflagration-to-detonation occurs, the addition of  $^{22}\text{Ne}$  decreases the overall mass of Ni-peak elements, in addition to lowering the isotopic fraction of  $^{56}\text{Ni}$ .

Our results can be improved in several ways. First, the  $^{22}\text{Ne}$  may be partially consumed as  $^{12}\text{C}$  burning gradually heats the core of the white dwarf (Podsiadlowski et al., 2006) some  $\approx 10^3$  yr prior to flame ignition. This may further reduce the electron fraction of the white dwarf, but will also change the reaction flows in the flame front. At low densities the morphology of the flame becomes more complicated, as the flows responsible for reaching quasi-statistical equilibrium are no longer fast enough to keep up with the carbon burning. Indeed, at  $\rho \leq 10^8 \text{ g cm}^{-3}$ , the eigenfunction for the flux begins to show two maxima and the flame speed becomes more dependent on the ambient fuel temperature. Further studies with more realistic compositions and at lower ambient densities are ongoing and will be reported in a forthcoming publication.

# Chapter 5

## Compositional effects of surface detonation

### 5.1 Introduction

In this chapter we explore the nuclear-synthetic yields that result from a surface detonation on a carbon-oxygen white dwarf. In § 5.2 we describe the type of detonation we are modeling and our computational method. Section 5.3 presents the computed gradient. We provide a list of nuclides that show a clear gradient. We also show that there is also a gradient in velocity space for elemental Ni before concluding, in § 5.4, with a discussion of how our results can be improved.

### 5.2 The Explosion Model

A promising candidate for the SNe Ia explosion mechanism is the gravitationally confined detonation (GCD) model (Plewa et al., 2004). In this model, the carbon burning runaway within the convective core is postulated to occur in a small region displaced from the stellar center, which results in a highly buoyant flame bubble that

quickly rises to the stellar surface after burning only a few percent of the star during its ascent (e.g. Livne et al., 2005). When the buoyant ash, as well as unburned material pushed ahead of the rising flame bubble, erupts forth from the stellar core it is largely confined to the surface of the white dwarf by gravity, and becomes a strong surface flow which sweeps completely over the star, eventually converging at the antipode of the breakout location. The high temperatures and densities reached within the converging surface flow are sufficient to trigger a detonation which incinerates the mostly unburned C/O white dwarf.

The resulting nuclear-synthetic yield consists almost entirely of detonation burning products, and depends on how much the star has expanded by the time the detonation initiates. More highly expanded (hence lower density) cores at detonation result in a smaller fraction of Fe peak nuclei, less  $^{56}\text{Ni}$ , and consequently a larger fraction of intermediate mass elements (IMEs) due to incomplete relaxation to NSE. Therefore, lower luminosity (less  $^{56}\text{Ni}$  producing) explosions are accompanied by a larger yield of IMEs.

The expansion of the star prior to detonation is a result of the work done on the star by the rising flame bubble. Deflagrations which burn more mass prior to reaching the stellar surface excite higher amplitude pulsations and hence more expanded stars at the time of detonation. It has been found that the expansion of the star due to the deflagration is very well represented by the fundamental radial pulsation mode of the underlying white dwarf (see Fig. 2 and Fig. 12 in Meakin et al., 2009). Therefore, while it is essential to understand the nature of the deflagration so as to better understand the mapping between initial conditions and final outcomes, the range of outcomes due to the deflagration can be parameterized by the pulsation amplitude, resulting in a one parameter family of models. While the phase of the pulsation at the time of detonation is a second parameter, it plays a lesser role because the time for the detonation wave to completely incinerate the star is short compared to the

pulsation period.

In the explosion model discussed in this chapter, we initiate a detonation in the surface layer of a cold ( $T = 4 \times 10^7$  K) white dwarf of mass  $1.365 M_{\odot}$  which has been expanded according to its fundamental radial-pulsation mode by such an amplitude that it has a central density of  $2 \times 10^8 \text{ g cm}^{-3}$ . This expansion results in  $\sim 0.7 M_{\odot}$  of high density material ( $\rho > 1 \times 10^8 \text{ g cm}^{-3}$ ), which burns to NSE in the detonation (primarily as  $^{56}\text{Ni}$ ). The remaining  $0.6 M_{\odot}$  of material burns to IMEs, e.g. Si, S, Ca, and Ar, resulting in only a small amount of unburned C/O in the outermost layers. The detonation is initiated by heating a small spherical volume ( $\sim 4$  km in radius) within the surface layer of the expanded white dwarf where the density is  $10^7 \text{ g cm}^{-3}$ . The reactive-hydrodynamic simulation of the explosion was conducted using the FLASH code (Fryxell et al., 2000). The code framework and the included physics is identical to that described in Meakin et al. (2009), and a maximum resolution of 4 km is used. An in depth description of the detonation phase, which results in a homologously expanding remnant, can be found in Meakin et al. (2009). Detailed yields are calculated by post processing Lagrangian tracer particles included in the explosion calculation and are the primary focus of this chapter.

Our reaction network incorporates 493 nuclides from n to  $^{86}\text{Kr}$  (Table 5.1). We use the reaction rates from the Joint Institute for Nuclear Astrophysics REACLIB Database<sup>1</sup> (Rauscher & Thielemann, 2000; Sakharuk et al., 2006, and references therein); the light-element rates are mostly experimental and are from compilations such as Caughlan & Fowler (1988) and Iliadis et al. (2001). Weak reaction rates are taken from Fuller et al. (1982) and Langanke & Martínez-Pinedo (2001). Screening is incorporated using the formalism of Graboske et al. (1973). Although our treatment of screening does not preserve detailed balance (Calder et al., 2007) this does not affect our calculation since we are concerned only with nuclides that never reach

---

<sup>1</sup><http://groups.nsl.msu.edu/jina/reactlib/db/>

El.	A	El.	A	El.	A	El.	A
n							
H	1-3	Ne	17-28	K	35-46	Ni	50-73
He	3-4	Na	20-31	Ca	35-53	Cu	54-70
Li	6-8	Mg	20-33	Sc	40-53	Zn	55-72
Be	7, 9-11	Al	22-35	Ti	39-55	Ga	58-73
B	8, 10-14	Si	22-38	V	43-57	Ge	59-76
C	9-16	P	26-40	Cr	43-60	As	62-76
N	12-20	S	27-42	Mn	46-63	Se	62-82
O	13-20	Cl	31-44	Fe	46-66	Br	71-81
F	15-24	Ar	31-47	Co	50-67	Kr	71-86

Table 5.1: 493-Nuclide Reaction Network

nuclear statistical equilibrium.

### 5.3 Results

We now present the results of our reaction network calculations for a surface detonation in a SN Ia model. We find that a number of nuclides exhibit a gradient throughout the stellar remnant. We determined this by plotting the final abundances of the various nuclides versus the final abundance of  $^{28}\text{Si}$ .  $^{28}\text{Si}$  is one of the most abundant species in the regime that does not reach nuclear statistical equilibrium. By plotting the final abundances of the nuclides versus the final abundance of  $^{28}\text{Si}$  we can separate out the particles we are interested in. We are interested in material that never reaches equilibrium and therefore is most affected by its thermal history. We then separate the particles into groups by the ejection angle. For these groups we chose particles ejected between  $+90^\circ$  and  $+60^\circ$ , between  $+15^\circ$  and between  $-15^\circ$ , and between  $-60^\circ$  and  $-90^\circ$ . In this system the detonation was prescribed to happen on the surface of the star in the  $+90^\circ$  direction. Any nuclide that showed greater than a 10% separation in the abundance between the different ejection angles was considered as having a gradient. Table 5.2 shows a partial listing of the nuclides that

separation	no separation
$^{57}\text{Ni}$	$^{56}\text{Ni}$
$^{55}\text{Co}$	$^{28}\text{Si}$
$^{55}\text{Ni}$	$^{32}\text{S}$
$^{58}\text{Ni}$	$^{52}\text{Fe}$
$^{60}\text{Zn}$	$^{48}\text{Cr}$
$^{34}\text{Ar}$	$^{24}\text{Mg}$
$^{30}\text{S}$	$^{39}\text{K}$
$^{29}\text{P}$	$^{15}\text{O}$
$^{53}\text{Fe}$	$^{27}\text{Si}$
$^{58}\text{Cu}$	
$^{59}\text{Cu}$	

Table 5.2: Partial table of nuclides that do and do not display a separation because of asymmetric detonation.

show a separation.

Our simulation is not run sufficiently past freeze out to allow all beta unstable nuclei to decay. If we force the unstable nuclei to decay, however, and group nuclei in elemental abundances, we find Ni to have the greatest gradient over the star. In material not burned to equilibrium we find the abundance of elemental Ni to increase by an order of magnitude between  $+90^\circ$  and  $-90^\circ$ . Figure 5.1 shows this dependence elemental Ni has on central angle.

We find that the composition gradient arises because of the extreme off center nature of the detonation. At first the shock wave from the detonation works with gravity compressing the fuel and leading to a longer thermal expansion time. We define a thermal expansion time  $t_{\text{exp}}$  as the time it takes a particle trajectory to go from it's maximum temperature  $T_{\text{max}}$  to a temperature of  $T_{\text{max}}e^{-1}$ . When the shock wave reaches the opposite side of the star the shock is now acting against the force of gravity helping to eject the material and leading to a shorter thermal expansion time. This difference in the thermal expansion time scales means material in the ejecta has different thermal histories as function of position (see Fig. 5.2.). These different

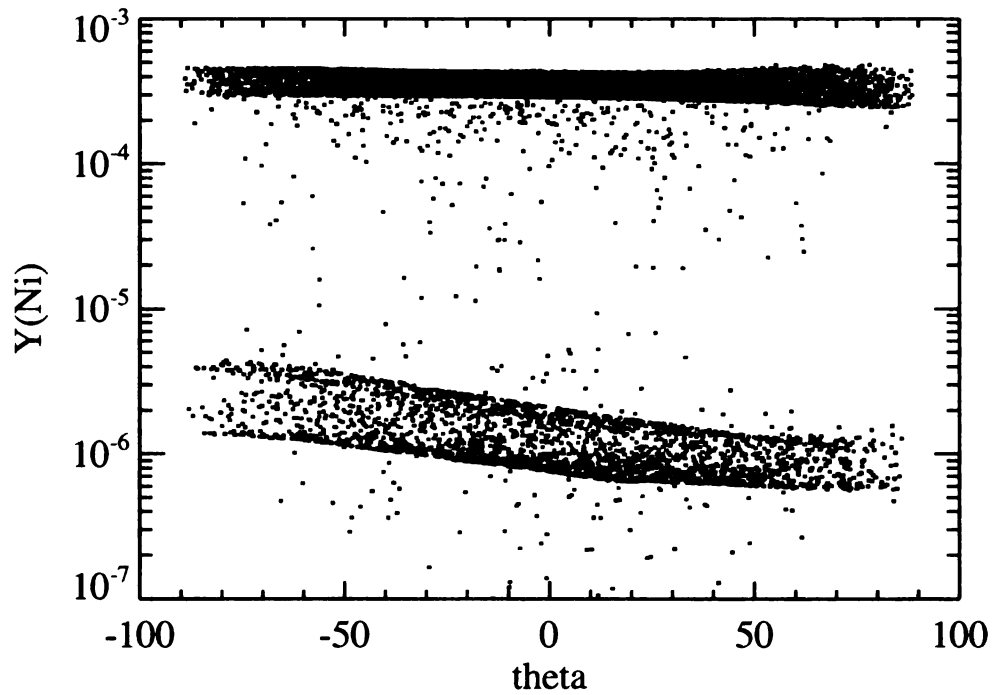


Figure 5.1: Final abundance of elemental Ni for each tracer, represented by a dot, as a function of the ejection angle relative to the center of the star for the tracer particles. The detonation occurred on the surface of the star in the  $\theta = 90$  direction. The particles with a Ni abundance above  $10^{-4}$  are particles that have burned to NSE.

thermal histories lead to the compositional gradient in the outer layers of the ejecta since the material never reaches NSE.

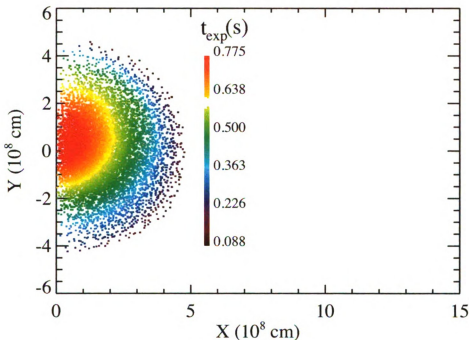


Figure 5.2: Initial spatial position of the tracer particles. Color represents each particles thermal expansion time scale. The center of the star is at  $Y=0$ ,  $X=0$ . The detonation was initiated at  $Y=5$ ,  $X=0$ . Particles on the side of the star where the detonation starts have higher thermal expansion time scales than the particles on the opposite side of the star.

An interesting side effect of the different expansion times is that material on opposite sides of the star will be expanding at different velocities. This leads to another effect where there is a gradient in velocity space. Figure 5.1 shows how elemental Ni varies with radial velocity. In material not burned to equilibrium the part of the remnant with the most Ni will also be the part with the highest radial velocity. This is self consistent since the Ni abundance is greater on the side of the remnant with the shortest expansion time therefore it follows it should have the highest radial velocity.

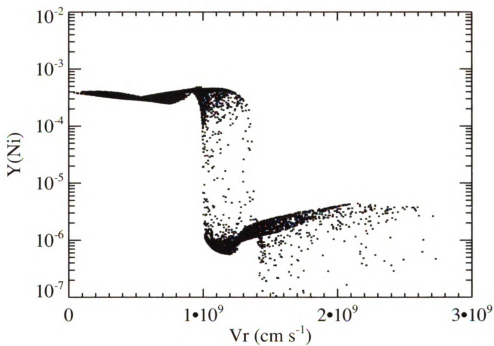


Figure 5.3: Final abundance of elemental Ni as a function of the final radial velocity. The particles with a Ni abundance above  $10^{-4}$  are particles that have burned to NSE. Particles with a Ni abundance less than  $10^{-5}$  show greater Ni abundance for larger radial velocities.

## 5.4 Discussion

We have computed the abundances and positions of nuclides created in a surface detonation in a SN Ia. We find a compositional gradient produced by the detonation in the ejecta. This compositional gradient is connected with the thermal expansion time scale since the burning never reaches nuclear statistical equilibrium and therefore the reactions that take place are dependent on the thermal history of the material. The different expansion timescales also result in there being a compositional gradient in velocity space.

Our results can be improved in several ways. First, light curves and spectra need to be generated to test the observational signature in more detail. It is currently unclear how much of an observation effect this compositional gradient has. A series of synthetic spectra generated over a range of time allows for direct comparison with observed supernovae. Even if any compositional effects are obscured, we conjecture, the spectra will see some dependence on observing angle since the side of the remnant that expands at higher velocities will also be at a lower density making it more transparent. The surface flow, which consists partly of deflagration ash, which was excluded from our the present model, needs to be considered. The surface flow might also have a spectral signature itself such as Fe peak material at high velocity and should be compared with the underlying compositional gradient.

# Chapter 6

## Conclusion

The principal use of this work will be in developing better large scale simulations of SNe Ia for comparison with observation. Simulating an entire Type Ia event from accretion to detonation using nothing more than first principals is currently too time intensive to be done on modern computers and it will be many years before this can even be considered. In the past SNe Ia models were often constructed with tunable parameters that could be adjusted until something resembling reality was produced. Whether or not these parameters corresponded to anything that physically happens is still an open question. More recent work has focused on simulating the physics that occurs on scales smaller than can be resolved by current SNe Ia models, so called sub-grid models. Sub-grid models tabulate much of the physics taking place and can be incorporated into the SNe Ia simulations in order for them have an improved theoretical robustness.

The simmering work in chapter 3 can be used to improve models of the SNe Ia prior to deflagration. Currently, doing nucleosynthesis calculations in a simulation of a simmering white dwarf is too computationally expensive. Given table 3.2 any individual wishing to simulate a simmering white dwarf needs only to keep track of how much carbon is burned in the simulation. Carbon burning requires only

one differential equation to evaluate and is much less computationally intensive than evaluating an entire reaction network. This will aid in research being done on the convective Urca process and on the start of deflagration. Energy loss from neutrinos in the convective Urca process may introduce a cooling term that is comparable to the heating term from the consumption of  $^{12}\text{C}$ . The amount of cooling that happens, and hence the amount of  $^{12}\text{C}$  burned, from convective Urca has varied considerably from publication to publication making a universally accepted prescription difficult (Stein et al., 1999; Lesaffre et al., 2005). Convective Urca may also effect the size and turnover time scale of the convective zone changing how much neutron rich material is made, and hence  $Y_e$  varies throughout the star. Future research will have to model how neutrino losses change the overall heating rate of the star as well as affect the convective zone. Knowing the exact composition at the end of simmering is ultimately necessary for exact modeling of the nucleosynthesis that happens afterwards, and therefore the final abundance of nuclides.

The work on flame speed in chapter 4 has been used to better understand the deflagration phase. SNe Ia simulations require a sub-grid model of the flame as an input parameter. This work is the first to provide a such a parameterization of a flame with  $^{22}\text{Ne}$  present. This parameterization can be incorporated into SNe Ia simulations to test compositional effects on SNe Ia events. In fact, this parameterization has already been included into code to test that very thing (Townesley et al., 2009). Studies recently done by Townesley et al. (2009) have looked at how  $^{22}\text{Ne}$  effects the dynamics of the expansion that happens before detonation. Their findings suggest that the presence of  $^{22}\text{Ne}$  does not effect the amount of  $^{56}\text{Ni}$  produced beyond that already predicted by Timmes et al. (2003) However all of the models in Townesley et al. (2009) assumed a transition to detonation at the exact same density. Depending on how a transition to detonation is defined in a model the transition may be dependent on the properties of the flame. At lower densities these properties become harder to define.

At densities above the expected detonation transition density the carbon and oxygen burning timescales significantly separate creating two flame like regions, one where carbon burns and another where everything else burns. At this point our original concepts of flame speed and width need to be reevaluated. Future work will have to focus on better understanding the flame at these low densities and as it transforms to a detonation. Ultimately, knowing exactly how the progenitor effects  $^{56}\text{Ni}$  production and hence the light curve will allow SNe Ia to be better used as standard candles.

Finally, the tracer particle calculations in chapter 5 can be used to determine the final outcome of a simulation in far better detail than before. SNe Ia simulations do not keep track of all nuclides. Knowing the distribution of all the nuclides relative to the ones kept track of in simulations will allow for publication of quick look-up tables for the composition of ejecta. Having an accurate composition of the ejecta will also allow for better simulated light curves and spectra to be plotted allowing for better comparisons between simulation and observation. This work can be extended to test the observational properties of different explosion models in more detail. Light curves and spectra need to be generated from the data to better compare with observation. The effects that surface flow has on the spectra and light curve also needs to be considered. If these steps are taken it may be possible in the future to determine the exact mechanism by which SNe Ia detonate, removing one of the unknowns behind these bright explosions in the sky.

# Bibliography

- Ajzenberg-Selove, F. 1991, *Nuclear Physics A*, 523, 1
- Anders, E. & Grevesse, N. 1989, *Geochim. Cosmochim. Acta*, 53, 197
- Asplund, M., Grevesse, N., & Sauval, A. J. 2005, in *Astronomical Society of the Pacific Conference Series*, Vol. 336, *Cosmic Abundances as Records of Stellar Evolution and Nucleosynthesis*, ed. T. G. Barnes, III & F. N. Bash, 25
- Badenes, C., Hughes, J. P., Bravo, E., & Langer, N. 2007, *ApJ*, 662, 472
- Bao, Z. Y. & Kappeler, F. 1987, *At. Data Nucl. Data Tables*, 36, 411
- Becerril Reyes, A. D., Gupta, S., Kratz, K. L., Möller, P., & Schatz, H. 2006, in *Nuclei in the Cosmos IX*, ed. J. Cederkäll et al. (Trieste: SISSA)
- Bildsten, L. 1995, *ApJ*, 438, 852
- Blondin, S., Dessart, L., Leibundgut, B., Branch, D., Höflich, P., Tonry, J. L., Matheson, T., Foley, R. J., Chornock, R., Filippenko, A. V., Sollerman, J., Spyromilio, J., Kirshner, R. P., Wood-Vasey, W. M., Clocchiatti, A., Aguilera, C., Barris, B., Becker, A. C., Challis, P., Covarrubias, R., Davis, T. M., Garnavich, P., Hicken, M., Jha, S., Krisciunas, K., Li, W., Miceli, A., Miknaitis, G., Pignata, G., Prieto, J. L., Rest, A., Riess, A. G., Salvo, M. E., Schmidt, B. P., Smith, R. C., Stubbs, C. W., & Suntzeff, N. B. 2006, *AJ*, 131, 1648
- Brown, B. A., Etchegoyen, A., Godwin, N. S., Rae, W. D. M., Richter, W. A., Ormand, W. E., Warburton, E. K., Winfield, J. S., Zhao, L., & Zimmerman, C. H. 2004, *OXBASH for Windows*, report 1289, MSU-NSCL
- Brown, E. F., Bildsten, L., & Chang, P. 2002, *ApJ*, 574, 920
- Brown, E. F., Calder, A. C., Plewa, T., Ricker, P. M., Robiinson, K., & Gallagher, J. B. 2005, *Nucl. Phys. A*, 758, 451
- Busso, M., Gallino, R., & Wasserburg, G. J. 1999, *ARA&A*, 37, 239

- Calder, A. C., Townsley, D. M., Seitenzahl, I. R., Peng, F., Messer, O. E. B., Vladimirova, N., Brown, E. F., Truran, J. W., & Lamb, D. Q. 2007, *ApJ*, 656, 313
- Cameron, A. G. W. 1959, *ApJ*, 130, 429
- Caughlan, G. R. & Fowler, W. A. 1988, *At. Data Nucl. Data Tables*, 40, 283
- Chamulak, D. A., Brown, E. F., & Timmes, F. X. 2007, *ApJ*, 655, L93
- Chou, W.-T., Warburton, E. K., & Brown, B. A. 1993, *Phys. Rev. C*, 47, 163
- Cohen, S. & Kurath, D. 1967, *Nuclear Physics A*, 101, 1
- Domínguez, I., Höflich, P., & Straniero, O. 2001, *ApJ*, 557, 279
- Feltzing, S., Holmberg, J., & Hurley, J. R. 2001, *A&A*, 377, 911
- Filippenko, A. V. 1997, *ARA&A*, 35, 309
- Fryxell, B., Olson, K., Ricker, P., Timmes, F. X., Zingale, M., Lamb, D. Q., MacNeice, P., Rosner, R., Truran, J. W., & Tufo, H. 2000, *ApJS*, 131, 273
- Fuller, G. M., Fowler, W. A., & Newman, M. J. 1982, *ApJS*, 48, 279
- Gallagher, J. S., Garnavich, P. M., Berlind, P., Challis, P., Jha, S., & Kirshner, R. P. 2005, *ApJ*, 634, 210
- Gallagher, J. S., Garnavich, P. M., Caldwell, N., Kirshner, R. P., Jha, S. W., Li, W., Ganeshalingam, M., & Filippenko, A. V. 2008, *ApJ*, 685, 752
- Gallino, R., Arlandini, C., Busso, M., Lugaro, M., Travaglio, C., Straniero, O., Chieffi, A., & Limongi, M. 1998, *ApJ*, 497, 388
- Gamezo, V. N., Khokhlov, A. M., & Oran, E. S. 2004, *Phys. Rev. Lett.*, 92, 211102
- Gasques, L. R., Afanasjev, A. V., Aguilera, E. F., Beard, M., Chamon, L. C., Ring, P., Wiescher, M., & Yakovlev, D. G. 2005, *Phys. Rev. C*, 72, 025806
- Graboske, H. C., Dewitt, H. E., Grossman, A. S., & Cooper, M. S. 1973, *ApJ*, 181, 457
- Hamuy, M., Trager, S. C., Pinto, P. A., Phillips, M. M., Schommer, R. A., Ivanov, V., & Suntzeff, N. B. 2000, *AJ*, 120, 1479
- Herwig, F. 2005, *ARA&A*, 43, 435
- Hillebrandt, W. & Niemeyer, J. C. 2000, *ARA&A*, 38, 191
- Höflich, P., Gerardy, C. L., Fesen, R. A., & Sakai, S. 2002, *ApJ*, 568, 791

- Höflich, P., Khokhlov, A. M., & Wheeler, J. C. 1995, *ApJ*, 444, 831
- Höflich, P., Wheeler, J. C., & Thielemann, F. K. 1998, *ApJ*, 495, 617
- Howell, D. A., Sullivan, M., Brown, E. F., Conley, A., LeBorgne, D., Hsiao, E. Y., Astier, P., Balam, D., Balland, C., Basa, S., Carlberg, R. G., Fouchez, D., Guy, J., Hardin, D., Hook, I. M., Pain, R., Perrett, K., Pritchett, C. J., Regnault, N., Baumont, S., LeDu, J., Lidman, C., Perlmutter, S., Suzuki, N., Walker, E. S., & Wheeler, J. C. 2009, *ApJ*, 691, 661
- Howell, D. A., Sullivan, M., Conley, A., & Carlberg, R. 2007, *ApJ*, 667, L37
- Iben, Jr., I. 1975, *ApJ*, 196, 525
- Iliadis, C., D'Auria, J. M., Starrfield, S., Thompson, W. J., & Wiescher, M. 2001, *ApJS*, 134, 151
- Iwamoto, K., Brachwitz, F., Nomoto, K., Kishimoto, N., Umeda, H., Hix, W. R., & Thielemann, F. 1999, *ApJS*, 125, 439
- Izzard, R. G., Lugaro, M., Karakas, A. I., Iliadis, C., & van Raai, M. 2007, *A&A*, 466, 641
- Jordan, IV, G. C., Fisher, R. T., Townsley, D. M., Calder, A. C., Graziani, C., Asida, S., Lamb, D. Q., & Truran, J. W. 2008, *ApJ*, 681, 1448
- Karakas, A. I., Lugaro, M. A., Wiescher, M., Görres, J., & Ugalde, C. 2006, *ApJ*, 643, 471
- Khokhlov, A. M. 1988, *Ap&SS*, 149, 91
- . 1995, *ApJ*, 449, 695
- Kuhlen, M., Woosley, S. E., & Glatzmaier, G. A. 2006, *ApJ*, 640, 407
- Langanke, K. & Martínez-Pinedo, G. 2001, *At. Data Nucl. Data Tables*, 79, 1
- Lattanzio, J. C. & Boothroyd, A. I. 1997, in *American Institute of Physics Conference Series*, Vol. 402, *American Institute of Physics Conference Series*, ed. T. J. Bernatowicz & E. Zinner, 85
- Leibundgut, B. 2001, *ARA&A*, 39, 67
- Lesaffre, P., Han, Z., Tout, C. A., Podsiadlowski, P., & Martin, R. G. 2006, *MNRAS*, 368, 187
- Lesaffre, P., Podsiadlowski, P., & Tout, C. A. 2005, *MNRAS*, 356, 131
- Liang, Y. C., Yin, S. Y., Hammer, F., Deng, L. C., Flores, H., & Zhang, B. 2006, *ApJ*, 652, 257

- Livne, E., Asida, S. M., & Höflich, P. 2005, *ApJ*, 632, 443
- Marion, G. H., Höflich, P., Wheeler, J. C., Robinson, E. L., Gerardy, C. L., & Vacca, W. D. 2006, *ApJ*, 645, 1392
- Marion, J. B. & Fowler, W. A. 1957, *ApJ*, 125, 221
- Mazzali, P. A. & Podsiadlowski, P. 2006, *MNRAS*, 369, L19
- Meakin, C. A., Seitzzahl, I., Townsley, D., Jordan, G. C., Truran, J., & Lamb, D. 2009, *ApJ*, 693, 1188
- Niemeyer, J. C. & Woosley, S. E. 1997, *ApJ*, 475, 740
- Paczynski, B. 1972, *Astrophys. Lett.*, 11, 53
- Phillips, M. M. 1993, *ApJ*, 413, L105
- Pinto, P. A. & Eastman, R. G. 2000, *ApJ*, 530, 744
- Piro, A. L. & Bildsten, L. 2008, *ApJ*, 673, 1009
- Plewa, T. 2007, *ApJ*, 657, 942
- Plewa, T., Calder, A. C., & Lamb, D. Q. 2004, *ApJ*, 612, L37
- Podsiadlowski, P., Mazzali, P. A., Lesaffre, P., Wolf, C., & Forster, F. 2006, *ArXiv Astrophysics e-prints*
- Press, W. H., Teukolsky, S. A., Vetterling, W. T., & Flannery, B. P. 1992, *Numerical Recipes in FORTRAN* (Cambridge: Cambridge University Press)
- Ramírez, I., Allende Prieto, C., & Lambert, D. L. 2007, *A&A*, 465, 271
- Rauscher, T. & Thielemann, F. 2000, *At. Data Nucl. Data Tables*, 75, 1
- Reeves, H. & Salpeter, E. E. 1959, *Physical Review*, 116, 1505
- Reinecke, M., Hillebrandt, W., & Niemeyer, J. C. 2002, *A&A*, 391, 1167
- Reinecke, M., Hillebrandt, W., Niemeyer, J. C., Klein, R., & Gröbl, A. 1999, *A&A*, 347, 724
- Riess, A. G., Strolger, L., Tonry, J., Casertano, S., Ferguson, H. C., Mobasher, B., Challis, P., Filippenko, A. V., Jha, S., Li, W., Chornock, R., Kirshner, R. P., Leibundgut, B., Dickinson, M., Livio, M., Giavalisco, M., Steidel, C. C., Benítez, T., & Tsvetanov, Z. 2004, *ApJ*, 607, 665
- Rolfs, C. E. & Rodney, W. S. 1988, *Cauldrons in the cosmos: Nuclear astrophysics* (Chicago, IL: University of Chicago Press)

- Röpke, F. K., Gieseler, M., Reinecke, M., Travaglio, C., & Hillebrandt, W. 2006, *A&A*, 453, 203
- Röpke, F. K. & Hillebrandt, W. 2004, *A&A*, 420, L1
- Röpke, F. K., Hillebrandt, W., Schmidt, W., Niemeyer, J. C., Blinnikov, S. I., & Mazzali, P. A. 2007a, *ApJ*, 668, 1132
- Röpke, F. K., Woosley, S. E., & Hillebrandt, W. 2007b, *ApJ*, 660, 1344
- Rowland, C., Iliadis, C., Champagne, A. E., Fox, C., José, J., & Runkle, R. 2004, *ApJ*, 615, L37
- Sakharuk, A., Elliot, T., Fisker, J. L., Hemingray, S., Kruiuzenga, A., Rauscher, T., Schatz, H., Smith, K., Thielemann, F.-K., & Wiescher, M. 2006, in *CAPTURE GAMMA-RAY SPECTROSCOPY AND RELATED TOPICS: 12th International Symposium*, ed. A. Woehr & A. Aprahamian, Vol. 819 (AIP), 118–122
- Salpeter, E. E. & Van Horn, H. M. 1969, *ApJ*, 155, 183
- Stein, J., Barkat, Z., & Wheeler, J. C. 1999, *ApJ*, 523, 381
- Stein, J. & Wheeler, J. C. 2006, *ApJ*, 643, 1190
- Sullivan, M., Le Borgne, D., Pritchett, C. J., Hodsman, A., Neill, J. D., Howell, D. A., Carlberg, R. G., Astier, P., Aubourg, E., Balam, D., Basa, S., Conley, A., Fabbro, S., Fouchez, D., Guy, J., Hook, I., Pain, R., Palanque-Delabrouille, N., Perrett, K., Regnault, N., Rich, J., Taillet, R., Baumont, S., Bronder, J., Ellis, R. S., Filiol, M., Lusset, V., Perlmutter, S., Ripoche, P., & Tao, C. 2006, *ApJ*, 648, 868
- Timmes, F. X. 1999, *ApJS*, 124, 241
- Timmes, F. X., Brown, E. F., & Truran, J. W. 2003, *ApJ*, 590, L83
- Timmes, F. X. & Woosley, S. E. 1992, *ApJ*, 396, 649
- Townsley, D. M., Jackson, A. P., Calder, A. C., Chamulak, D. A., Brown, E. F., & Timmes, F. X. 2009, *ApJ*, 701, 1582
- Travaglio, C., Hillebrandt, W., Reinecke, M., & Thielemann, F.-K. 2004, *A&A*, 425, 1029
- Tremonti, C. A., Heckman, T. M., Kauffmann, G., Brinchmann, J., Charlot, S., White, S. D. M., Seibert, M., Peng, E. W., Schlegel, D. J., Uomoto, A., Fukugita, M., & Brinkmann, J. 2004, *ApJ*, 613, 898
- Woosley, S. E., Kasen, D., Blinnikov, S., & Sorokina, E. 2007, *ApJ*, 662, 487
- Woosley, S. E., Wunsch, S., & Kuhlen, M. 2004, *ApJ*, 607, 921

- Yakovlev, D. G., Gasques, L. R., Afanasjev, A. V., Beard, M., & Wiescher, M. 2006, *Phys. Rev. C*, 74, 035803
- Zegers, R. G. T., Brown, E. F., Akimune, H., Austin, S. M., van den Berg, A. M., Brown, B. A., Chamulak, D. A., Fujita, Y., Galès, S., Harakeh, M. N., Hashimoto, H., Hayami, R., Hitt, G. W., Itoh, M., Kawabata, T., Kawase, K., Kinoshita, M., Nakanishi, K., Nakayama, S., Okamura, S., Shimbara, Y., Uchida, M., Ueno, H., Yamagata, T., & Yosoi, M. 2007, *Phys. Rev. C*, submitted
- Zhang, J., Messer, O. E. B., Khokhlov, A. M., & Plewa, T. 2006, *ApJ*, in press
- Zingale, M. & Dursi, L. J. 2007, *ApJ*, 656, 333
- Zingale, M., Woosley, S. E., Rendleman, C. A., Day, M. S., & Bell, J. B. 2005, *ApJ*, 632, 1021

MICHIGAN STATE UNIVERSITY LIBRARIES



3 1293 03062 9384